Article

Insufficiency of ciliary cholesterol in hereditary Zellweger syndrome

Tatsuo Miyamoto[1,*,†] iD, Kosuke Hosoba[1,2,†], Takeshi Itabashi[3], Atsuko H Iwane[3], Silvia Natsuko Akutsu[1], Hiroshi Ochiai[2] iD, Yumiko Saito[2,4], Takashi Yamamoto[2,5] & Shinya Matsuura[1,**] iD

Abstract

Primary cilia are antenna-like organelles on the surface of most mammalian cells that receive sonic hedgehog (Shh) signaling in embryogenesis and carcinogenesis. Cellular cholesterol functions as a direct activator of a seven-transmembrane oncoprotein called Smoothened (Smo) and thereby induces Smo accumulation on the ciliary membrane where it transduces the Shh signal. However, how cholesterol is supplied to the ciliary membrane remains unclear. Here, we report that peroxisomes are essential for the transport of cholesterol into the ciliary membrane. Zellweger syndrome (ZS) is a peroxisome-deficient hereditary disorder with several ciliopathy-related features and cells from these patients showed a reduced cholesterol level in the ciliary membrane. Reverse genetics approaches revealed that the GTP exchange factor Rabin8, the Rab GTPase Rab10, and the microtubule minus-end-directed kinesin KIFC3 form a peroxisome-associated complex to control the movement of peroxisomes along microtubules, enabling communication between peroxisomes and ciliary pocket membranes. Our findings suggest that insufficient ciliary cholesterol levels may underlie ciliopathies.

Introduction

Primary cilia are microtubule (MT)-based, nonmotile organelles located on the surface of most mammalian cells, which sense extracellular information to transduce signals required for embryonic development and adult tissue homeostasis (Nigg & Raff, 2009;

Ishikawa & Marshall, 2011). Germline mutations of primary cilium-associated genes cause ciliopathies characterized by a range of clinical features, including polycystic kidney, polydactyly, retinitis pigmentosa, obesity, mental retardation, and neuronal and other developmental abnormalities (Baker & Beales, 2009). To date, at least 35 ciliopathies have been established. According to recent proteomic and human genetic analyses, more than 240 candidate ciliopathy-related genes are associated with ciliary structures and/or functions that cause known or unique ciliopathies if mutated in humans (Reiter & Leroux, 2017).

The vertebrate sonic hedgehog (Shh) signal is interpreted by primary cilia (Goetz & Anderson, 2010). In the absence of the Shh ligand, its receptor patched1 (Ptc1) localizes to primary cilia to silence downstream factors such as Gli transcription factors. During Shh stimulation, the ligand binds to Ptc1 to promote the ciliary exit of Ptc1 and the ciliary entry of Smoothened (Smo), thereby translocating the Gli transcription factors from the primary cilia to the nucleus to activate target gene expression (Corbit *et al*, 2005; Rohatgi *et al*, 2007). Insufficient Shh signal transduction in embryogenesis causes congenital malformations such as holoprosencephaly, cerebellar hypoplasia, and polydactyly overlapping with the clinical spectrum of ciliopathies (Ming *et al*, 1998; Muenke & Beachy, 2000; Varjosalo *et al*, 2006), while the hyperactivation after birth is involved in carcinogenesis including basal carcinoma and medulloblastoma (Teglund & Toftgard, 2010). With respect to the link between Shh signaling and ciliary membrane lipid composition, cellular cholesterol directly binds to Smo to orchestrate the Shh transcriptional program (Byrne *et al*, 2016; Huang *et al*, 2016, 2018; Luchetti *et al*, 2016; Myers *et al*, 2017; Xiao *et al*, 2017), suggesting that cholesterol might be essential for the functions of primary cilia. Indeed, germline mutations of the cholesterol biosynthetic enzyme *DHCR7* in Smith–Lemli–Opitz syndrome (SLOS, MIM: 270400) lead to congenital abnormalities including micrognathia, cleft palate, holoprosencephaly, syndactyly, polydactyly, and polycystic kidney (Fitzky *et al*, 1998; Wassif *et al*, 1998; Matsumoto *et al*, 2005;

1   Department of Genetics and Cell Biology, Research Institute for Radiation Biology and Medicine, Hiroshima University, Hiroshima, Japan
2   Program of Biomedical Science, Graduate School of Integrated Sciences for Life, Hiroshima University, Higashi-Hiroshima, Japan
3   Laboratory for Cell Field Structure, RIKEN Center for Biosystems Dynamics Research, Higashi-Hiroshima, Japan
4   Program of Life and Environmental Sciences, Graduate School of Integrated Sciences for Life, Hiroshima University, Higashi-Hiroshima, Japan
5   Program of Mathematical and Life Sciences, Graduate School of Integrated Sciences for Life, Hiroshima University, Higashi-Hiroshima, Japan
    *Corresponding author. Tel: +81 82 257 5811; Fax: +81 82 256 7101; E-mail: t-miyamoto@hiroshima-u.ac.jp
    **Corresponding author. Tel: +81 82 257 5809; Fax: +81 82 256 7101; E-mail: shinya@hiroshima-u.ac.jp
    †These authors contributed equally to this work

Nowaczyk & Irons, 2012), implying that a low level of cellular cholesterol might cause ciliopathies.

Mammalian cells synthesize cholesterol in the endoplasmic reticulum (ER) *de novo* and acquire it via receptor-mediated endocytosis of low-density lipoprotein (LDL; Simons & Ikonen, 2000). Cellular cholesterol is dynamically transported and unevenly distributed in the intracellular membranes (Ikonen, 2008). Only ~0.5–1% of total cellular cholesterol is present in the ER membrane (Lange *et al*, 1999), while its concentration is highest at ~60–80% in the plasma membrane (PM; Liscum & Faust, 1989). Cholesterol is also chemically modified in different organelles. For example, it is esterified in the ER for storage and converted to steroids and bile acids in mitochondria and peroxisomes (Vance & Vance, 1990; Ishibashi *et al*, 1996; Chang *et al*, 1997). Dynamic intracellular trafficking of cholesterol is thus important for its physiological roles. LDL-derived cholesterol trafficking is the best-known route of intracellular cholesterol transport in most mammalian cells (Brown & Goldstein, 1986). Upon the binding of plasma LDL to its receptor and subsequent internalization, LDL is delivered from early endosome to late endosome/lysosome, where LDL-derived cholesterol esters are hydrolyzed by lysosomal acid lipase to free cholesterol. Free cholesterol then egresses from late endosome/lysosome to be targeted into downstream organelles, including PM, ER, peroxisomes, and mitochondria (Ikonen, 2008; Chu *et al*, 2015). A series of studies of the hereditary neurodegenerative disorder Niemann–Pick type C (NPC) syndrome (MIM: 607623 and 607625) caused by germline mutation of the *NPC1* or *NPC2* gene have provided the most mechanistic knowledge on the egress of free cholesterol from late endosome/lysosome to other organelles (Carstea *et al*, 1997; Naureckiene *et al*, 2000). NPC2 binds free cholesterol in the lysosomal lumen to deliver it to the membrane-bound NPC1 (Sleat *et al*, 2004). In the route of free cholesterol egress from late endosome/lysosome to the PM, one type of regulatory machinery involved is small GTPase Rab8a-mediated vesicular trafficking along the actin filaments (Kanerva *et al*, 2013).

It has been reported that the cholesterol in the ciliary membranes is distinctively abundant compared with the level in the rest of the PM (Chailley *et al*, 1983; Chailley & Boisvieux-Ulrich, 1985). In contrast, other studies have failed to detect the enrichment of cholesterol in the ciliary membranes (Breslow *et al*, 2013; Kinnebrew *et al*, 2019). In many cell types, the basal part of primary cilia is embedded within a membrane invagination called the ciliary pocket, which compartmentalizes the ciliary membrane from the rest of the PM (Molla-Herman *et al*, 2010; Benmerah, 2013). Although the cells of NPC patients exhibit lower formation of cilia and notable accumulation of cholesterol in the lysosomal lumen to severely reduce the cholesterol level in the PM (Formichi *et al*, 2018), most NPC patients do not show typical ciliopathy-related symptoms. These findings imply the existence of unknown trafficking routes of cellular cholesterol into the primary cilium membrane.

Peroxisomes are single-membrane-bounded organelles that perform various physiological functions, including α- and β-oxidation of fatty acids, amino acid synthesis, and metabolism of reactive oxygen species (ROS) and bile acids (Wanders, 2014). ZS is an autosomal recessive peroxisome biogenesis disorder (PBD) caused by germline mutations of the 13 known peroxisomal biogenesis factor (*PEX*) genes, which encode proteins called peroxins (Fujiki, 2016).

Among these, *PEX1* (~60%; MIM: 602136) encoding AAA$^+$ ATPase for the assembly of peroxisomes is the most commonly defective (Portsteffen *et al*, 1997; Reuber *et al*, 1997). Patients with ZS show various clinical features from mild to early lethal, ranging from mild neurosensory defects to severe neonatal hypotonia and liver dysfunction (Argyriou *et al*, 2016; Waterham *et al*, 2016). They also often exhibit polycystic kidney and retinitis pigmentosa (Luisiri *et al*, 1988; Folz & Trobe, 1991; FitzPatrick, 1996; Klouwer *et al*, 2015), suggesting a possible correlation of peroxisome gene mutations with ciliopathies. Recently, it was reported that peroxisomes contact lysosomes to control intracellular cholesterol trafficking and that the cells of patients with ZS show massive accumulation of cholesterol in the cytoplasm (Chu *et al*, 2015). Although polycystic kidney and retinitis pigmentosa observed in ZS are not the typical defects in Shh pathway and cholesterol biosynthesis, ZS-related pathological links between the ciliopathy-associated symptoms and the intracellular excess accumulation of cholesterol led us to explore how peroxisomes regulate the physiological roles of primary cilia via intracellular cholesterol.

In this study, we demonstrate that skin fibroblasts from ZS patients and *PEX1*- and *PEX14*-deficient hTERT-immortalized human retinal pigment epithelial (hTERT-RPE1) cells generated using CRISPR/Cas9 technology show a reduced level of cholesterol in the ciliary membranes and dampened Shh signal transduction. Using time-lapse imaging, we observed that peroxisomes as a carrier of cholesterol move along the microtubules to contact the ciliary pocket membranes. We also identified that the Rabin8–Rab10–KIFC3 complex is involved in the peroxisome-mediated trafficking of cholesterol to the primary cilia.

Results

Cholesterol in the ciliary membrane is insufficient in ZS

Patients with ZS often exhibit ciliopathy-associated features such as polycystic kidney and retinitis pigmentosa (Luisiri *et al*, 1988; Folz & Trobe, 1991; FitzPatrick, 1996; Klouwer *et al*, 2015). We thus speculated that ZS involves ciliary dysfunction. Primary skin fibroblasts from two unrelated ZS patients with mutation of either the *PEX1* or the *PEX26* gene were synchronized by serum starvation at the quiescent G_0 phase and observed for the formation of primary cilia. They were ciliated as much as cells from a normal individual (Appendix Fig S1A and B), suggesting that peroxisomes are dispensable for ciliogenesis. In agreement with a previous study (Chu *et al*, 2015), the ZS patients' cells displayed the massive intracellular accumulation of cholesterol as with cells from an X-linked adrenoleukodystrophy (X-ALD) patient with peroxisomal lipid transporter *ABCD1* mutation and an NPC patient (Appendix Fig S1F). In contrast to the reduced amounts of total and free cholesterol in the SLOS patient's cells compared with those in cells from a normal individual, total cholesterol levels in ZS, X-ALD and NPC patients' cells and free cholesterol levels in X-ALD and NPC patients' cells were significantly increased (Appendix Fig S1D and E). Since the involvement of cholesterol in cilium-dependent Shh signaling has been suggested, we then examined the localization of cholesterol in cilia in patient cells by staining with a cholesterol probe, Filipin III. In the ZS patients' cells, there was a significant decrease in ciliary

cholesterol, like in the SLOS patient's cells (Fig 1A and B). Interestingly, this level was not affected in cells from the X-ALD and NPC patients without conditions on the cilium-related disease spectrum (Fig 1A and B), implying that the supply of cholesterol to the ciliary membrane is independent of the well-known NPC1-mediated cholesterol trafficking route.

Next, we investigated whether peroxisomes are required for Shh signaling. Stimulating normal individual cells with the N-terminal signaling portion of Shh, Shh-N, effectively enhanced the ciliary localization of Smo (Fig 1C–E). To evaluate the Shh signal transduction, we monitored the elevated transcription of the Shh target gene *Gli1* induced by the Smo agonist SAG (Hui & Angers, 2011; Garcia-Gonzalo *et al*, 2015; Blassberg *et al*, 2016; Appendix Fig S1C). These responses were impaired in the cells of SLOS and ZS patients, but not in those of X-ALD and NPC1 patients, indicating the role of peroxisomes in activating Shh signal transduction (Fig 1C–E). To investigate whether the dampened Shh signaling in the cells of ZS patients is attributable to the insufficient ciliary cholesterol, we analyzed the effects of exogenous cholesterol on the ciliary accumulation of Smo in patient cells stimulated with Shh-N. As expected, cholesterol depletion using methyl-β-cyclodextrin inhibited the ciliary accumulation of Smo even in the cells from a normal individual (Fig 1F and G), demonstrating that cellular cholesterol is required for the ciliary entry of Smo. Culturing the cells from SLOS and ZS patients in the presence of exogenous cholesterol (cholesterol/methyl-β-cyclodextrin complex), which is thought to directly provide cholesterol to the cellular membranes (Lopez *et al*, 2011), and a cholesterol biosynthesis inhibitor, pravastatin, restored the reduced Shh-N-induced ciliary accumulation of Smo to the level in the cells from a normal individual (Fig 1F and G). In contrast, the LDL-mediated compensation at an incorporated cholesterol amount similar to that with 100 μM cholesterol/methyl-β-cyclodextrin complex rescued the defect in Shh-N-induced ciliary Smo localization in SLOS patient-derived cells, but not perfectly in the cells from ZS patients (Fig 1F and G, Appendix Fig S1G). The cholesterol incorporation occurred with similar efficacy among the treated cells, suggesting that the difference of ciliary Smo localization might not be attributable to the variation of cholesterol incorporation (Appendix Fig S1G). These findings demonstrate that the defect in intracellular cholesterol trafficking causes the reduced level of ciliary cholesterol to perturb the Shh signal transduction in ZS.

CRISPR/Cas9-mediated disruption of *PEX* genes in human cultured cell line confirms ciliary dysfunction

It is problematic to compare primary fibroblasts derived from different human patients under different conditions at different times and to limit further cell biological analyses in the primary fibroblasts because of their extremely low efficacy of transgene introduction. In addition to the PEX1–PEX26 biochemical complex, other *PEX* gene products are known to form distinct complexes in the context of peroxisome formation (Fujiki, 2016). To confirm that peroxisomes *per se* are indeed involved in the ciliary function, we attempted to disrupt the *PEX1* and *PEX14* genes in human ciliated hTERT-RPE1 cell lines with a uniform genetic background using the nonhomologous end-joining (NHEJ)-mediated targeting method named ObLiGaRe (obligate ligation-gated recombination; Maresca *et al*, 2013; Royba *et al*, 2017). In this method, cotransfection of

CRISPR/Cas9 and drug-resistant gene cassette vectors tagged with the CRISPR/Cas9 site located in the genome into hTERT-RPE1 cells enabled the generation of *PEX1*- and *PEX14*-knockout cell clones at more than 50% efficacy after drug selection (Appendix Tables S1 and S2). Western blotting and immunostaining analyses demonstrated no PEX1 and PEX14 products in the $PEX1^{-/-}$ and $PEX14^{-/-}$ hTERT-RPE1 cell clones (Fig 2A and B). Consistent with the observations of the fibroblasts derived from the ZS patients (Castro *et al*, 2018a), these clones also showed remarkably impaired peroxisome formation (Fig 2B and C). The PMP70 and ACOX1 (acyl-CoA oxidase 1)-double-positive peroxisomes were dramatically reduced in the $PEX1^{-/-}$ and $PEX14^{-/-}$ hTERT-RPE1 cell clones (Appendix Fig S2A), suggesting that they also had the defect in peroxisomal matrix protein import. Therefore, these knockout cell clones were successfully established as a model of ZS and used for subsequent studies.

The number and length of primary cilia were investigated in the serum-starved *PEX1*- and *PEX14*-knockout cells. They showed no significant alterations in ciliogenesis and melanin-concentrating hormone (MCH)-dependent ciliary shortening (Hamamoto *et al*, 2016) compared with wild-type (parental) cells (Fig 2D, Appendix Fig S2B and C). However, Filipin III staining analysis revealed that ciliary cholesterol was significantly insufficient in the $PEX1^{-/-}$ and $PEX14^{-/-}$ hTERT-RPE1 cells (Fig 2E and F). Since Filipin III can be affected by factors other than cholesterol level, we evaluated the ciliary cholesterol using fluorescently labeled Domain 4 (D4) of Perfringolysin O as another cholesterol probe (Ohno-Iwashita *et al*, 2004; Das *et al*, 2013) (Fig 2E and G, Appendix Fig S2D and E). In the parental hTERT-RPE1 cells, the signal intensity of AcGFP1-tagged D4 in the ciliary membrane was stronger than that in the rest of the plasma membrane (Appendix Fig S2D and E). Consistent with the Filipin III staining data, ciliary insufficiency and cytosolic accumulation of AcGFP1-tagged D4 in the $PEX1^{-/-}$ and $PEX14^{-/-}$ hTERT-RPE1 cells were observed (Fig 2E and G, Appendix Fig S2D and E), suggesting that peroxisomes are required for the enrichment of ciliary cholesterol and intracellular cholesterol trafficking. These mutant hTERT-RPE1 cells and the $PEX14^{-/-}$ NIH3T3 cells generated with the CRISPR-ObLiGaRe method also exhibited impaired ciliary accumulation of Smo following Shh-N stimulation (Fig 2H and I, Appendix Fig S3G–I, Appendix Table S1 and S2), while the *Pex14* deficiency did not affect the ciliary localization of Ptc1 (Appendix Fig S3A and B). These findings suggested that the peroxisome-mediated control of the ciliary Smo localization is conserved across multiple cell lines. These ciliary phenotypes in the $PEX14^{-/-}$ hTERT-RPE1 cells were complementary under the exogenous PEX14 gene expression (Appendix Fig S3C–F), suggesting that the *PEX* genes are essential for the appropriate response to Shh ligands. Notably, exogenous cholesterol (cholesterol/methyl-β-cyclodextrin complex), but not LDL, effectively led to the restoration of Shh-N-mediated ciliary accumulation of Smo in these knockout cells (Fig 2H and I, Appendix Fig S1H), suggesting that peroxisomes are involved in the supply of cholesterol into the ciliary membrane.

Processing of the Shh ligand from the full-length precursor to mature Shh-N is also controlled by cholesterol. To test whether disruption of the *PEX* genes impairs the maturation of the Shh ligand, we monitored the states of Shh protein in the $PEX1^{-/-}$ and $PEX14^{-/-}$ hTERT-RPE1 cells using Western blotting analysis. They
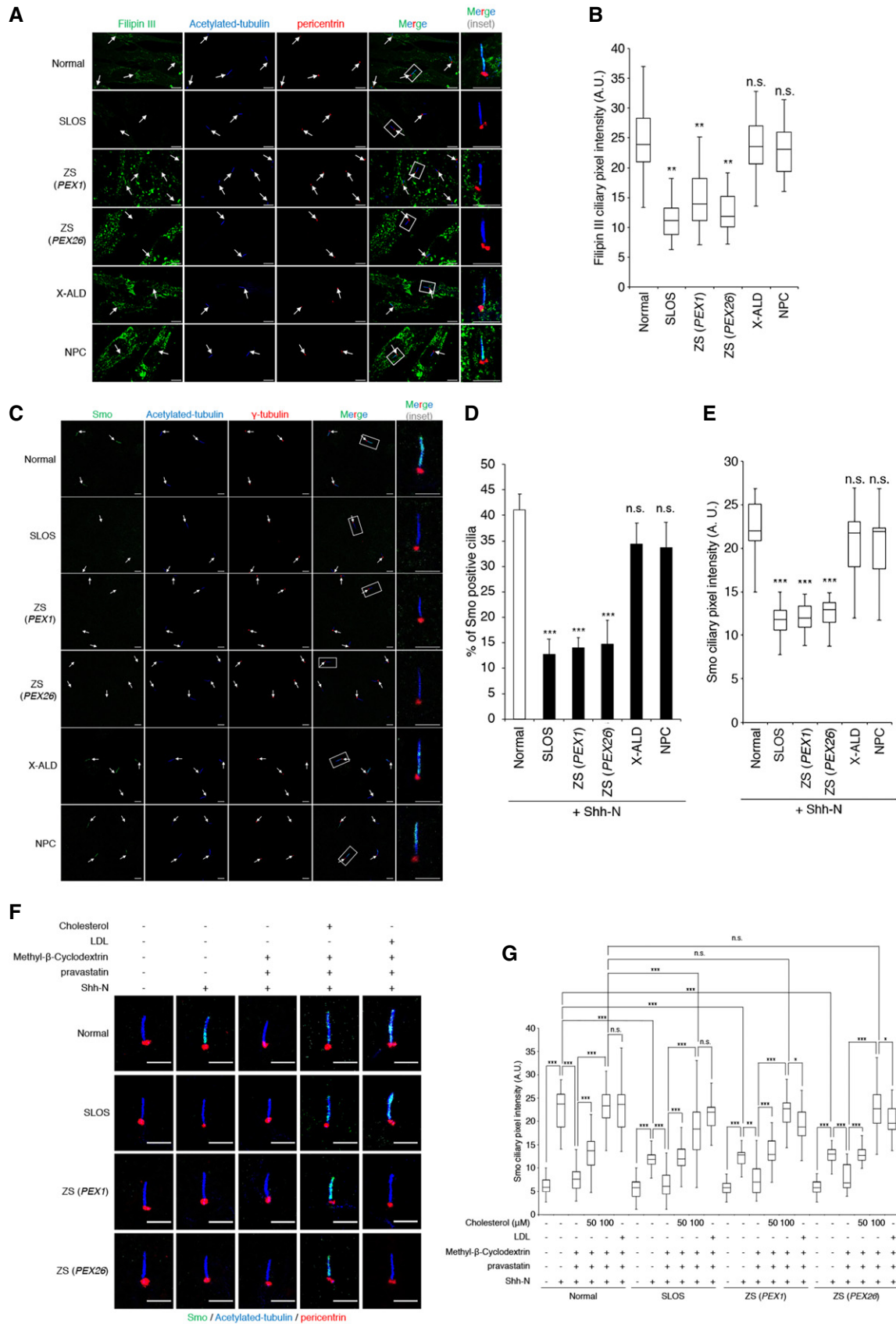
Figure 1.

◀

Figure 1.   Cells from ZS patients show defects in cholesterol enrichment in the ciliary membrane and Shh signal transduction.

A   Primary skin fibroblasts from a normal individual, SLOS patient, ZS patients, X-ALD patient, and NPC patient incubated for 24 h without serum were immunostained with anti-pericentrin (red) and anti-acetylated-tubulin (blue) antibodies. Cholesterol was stained with Filipin III (green). Arrows indicate primary cilia. Scale bar, 5 μm.

B   The intensity of Filipin III signal at primary cilia from (a) was remarkably reduced in SLOS and ZS patient cells (**$P < 0.01$: one-way ANOVA with Tukey's HSD, $n = 3$: 45–50 cells per experiment). In the boxplot, medians, $25^{th}/75^{th}$ percentile, and min/max were represented by the central lines, the box limits, and the whiskers/error bars, respectively.

C   Immunofluorescent staining of primary skin fibroblasts in quiescent G_0 phase treated with 50 nM Shh-N for 24 h using anti-Smo (green), anti-acetylated-tubulin (blue), and anti-γ-tubulin (red) antibodies. Arrows indicate primary cilia. Scale bar, 2.5 μm.

D   Quantification of proportion of Smo-positive ciliated cells upon Shh-N stimulation from (C). The populations of Smo-positive ciliated fibroblasts from the SLOS and ZS patients were significantly reduced (mean ± s.d.: ***$P < 0.001$: one-way ANOVA with Tukey's HSD, $n = 3$: 100 cells per experiment).

E   The Smo intensity at primary cilia in the fibroblasts from (C). The ciliary localization of Smo upon Shh-N stimulation was significantly impaired in fibroblasts from the SLOS and ZS patients (***$P < 0.001$: one-way ANOVA with Tukey's HSD, $n = 3$: 90–100 cells per experiment). In the boxplot, medians, $25^{th}/75^{th}$ percentile, and min/max were represented by the central lines, the box limits, and the whiskers/error bars, respectively.

F   Primary fibroblasts from a normal individual, and SLOS and ZS patients were treated with 1.5% methyl-β-cyclodextrin for 45 min to remove cellular cholesterol and then incubated with or without cholesterol (cholesterol/methyl-β-cyclodextrin complex) for 1 h. After washing out the exogenous cholesterol, the fibroblasts were stimulated with 50 nM Shh-N for 24 h in the presence of pravastatin and then immunostained with anti-Smo (green), anti-acetylated-tubulin (blue), and anti-pericentrin (red) antibodies. For the alternative cholesterol complementation, LDL (0.06 mg/ml) was co-incubated with Shh-N and pravastatin for 24 h after methyl-β-cyclodextrin-mediated cholesterol depletion. Scale bar, 2.5 μm.

G   Quantification of the Smo intensity at primary cilia in the fibroblasts from (F). The ciliary accumulation of Smo upon the Shh-N stimulation of fibroblasts from an SLO patient was restored by the complementation of both exogenous cholesterol/methyl-β-cyclodextrin complex and LDL, while that of cells from ZS patients was efficiently rescued by not LDL but cholesterol/methyl-β-cyclodextrin complex (*$P < 0.05$, **$P < 0.01$, ***$P < 0.001$: one-way ANOVA with Tukey's HSD, $n = 3$: 90–100 cells per experiment). In the boxplot, medians, $25^{th}/75^{th}$ percentile, and min/max were represented by the central lines, the box limits, and the whiskers/error bars, respectively.

exhibited no significant change in Shh protein processing compared with wild-type hTERT-RPE1 cells (Fig 2A), suggesting that the dampened Shh signaling in ZS is attributable to the ability to receive the Shh signal rather than the production of mature Shh ligand. These results confirm that the *PEX* genes play a role in the localization of ciliary cholesterol for transducing the Shh signals.

Peroxisomes contact the ciliary pocket in a microtubule-dependent manner

To explore how peroxisomes mediate the supply of cholesterol to the ciliary membrane, we first examined the subcellular distribution of cholesterol by performing Filipin III staining in serum-starved hTERT-RPE1 cells. Three-dimensional reconstitution analysis of confocal images demonstrated that Filipin III signals were located at the peripheral membrane regions of both the primary cilia and peroxisomes (Fig 3A), suggesting that peroxisomes might function as a carrier of cellular cholesterol to the ciliary membrane.

To test whether peroxisomes physically interact with primary cilia, we next observed the dynamics of peroxisomes by time-lapse cell imaging of the ciliary membrane receptor MCHR1-GFP, the basal body (centrosome) marker DsRed2-PACT (pericentrin-AKAP450 centrosomal targeting domain), and the peroxisomal targeting molecule ECFP-SKL in serum-starved hTERT-RPE1 cells. Approximately 10 independent contacts between peroxisome and primary cilium occurred in 2 h, and the contacts continued for 10–20 min in the untreated hTERT-RPE1 cells containing approximately 150–200 peroxisomes labeled with ECFP-SKL (Appendix Fig S4, Movie EV1). To precisely determine the spatial interaction between peroxisomes and primary cilia, we stained endogenous peroxisomes and primary cilia with anti-PMP70 (peroxisomes), anti-ninein (basal bodies), anti-ARL13B (ciliary axonemes), and anti-phospho Ser473 Akt (ciliary pockets) antibodies (Suizu *et al*, 2016). Some PMP70-positive spots partially overlapped with the phospho Ser473-Akt spot at the ciliary pocket in around 15% of the hTERT-RPE1 cell population (Fig 3B and C). 3D-structure illuminated microscopy (3D-SIM) also revealed that the PMP70-positive

peroxisomes contacted the ciliary pocket labeled with anti-phospho Ser473 Akt antibody (Appendix Fig S5A and B). Cilium-bound PMP70-positive peroxisomes were not detected in the upper axonemal compartment from the distal appendages labeled with anti-ODF2 antibody (Appendix Fig S5C). Three-dimensional focused ion beam scanning electron microscopy (FIB-SEM) combined with correlative light and electron microscopy (CLEM) revealed that peroxisomes labeled with ECFP-SKL associated with the ciliary pocket (Fig 4). Treatment of hTERT-RPE1 cells with Colcemid and Ciliobrevin-D, a microtubule depolymerizer and dynein motor inhibitor, respectively, did not alter the total number of peroxisomes, but impaired the dynamic contact between peroxisomes and cilia (Fig 3B and Appendix Fig S4, Movie EV3 and EV4), implying that microtubules might be required for peroxisome dynamics. In contrast, Cytochalasin-D, an actin depolymerizer, did not affect the contact (Fig 3B and Appendix Fig S4, Movie EV2), suggesting that actin filaments are dispensable for peroxisome dynamics. Consistent with the time-lapse imaging data, an immunostaining analysis revealed that the hTERT-RPE1 cell population with a PMP-70-positive signal merged with the phospho-Ser473 Akt signal at the ciliary pocket significantly decreased after the Colcemid and Ciliobrevin-D treatments, but not after the Cytochalasin-D treatment (Fig 3B). These results suggest that the dynamic contact between peroxisomes and primary cilia is dependent on microtubules.

To examine whether the microtubule-dependent dynamic contact between peroxisomes and cilia contributes to the supply of cholesterol into the ciliary membrane, we stained the Colcemid-, Ciliobrevin-D-, or Cytochalasin-D-treated hTERT-RPE1 cells with Filipin III. The signals of the surrounding plasma membrane in the cytoskeletal inhibitor-treated cells were reduced compared with those of the untreated cells (Fig 3D). The signals at the ciliary axonemal membrane were also significantly reduced in the Colcemid- and Ciliobrevin-treated cells, whereas they were clearly detected in the untreated and Cytochalasin-D-treated cells (Fig 3D and E). These findings suggested the involvement of the microtubule-dependent dynamic contact between peroxisomes and ciliary pockets in the trafficking of cholesterol to the ciliary membrane.
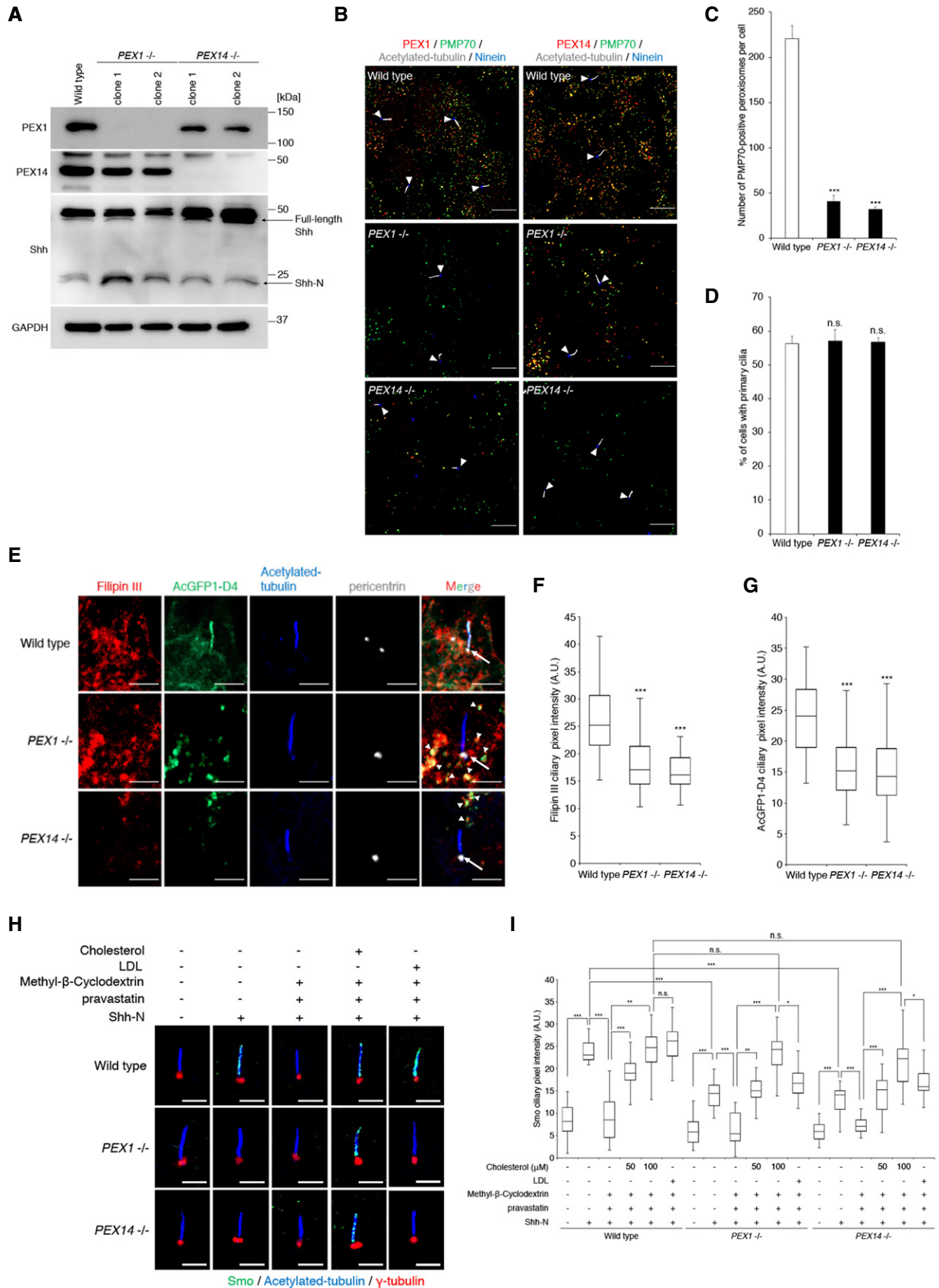
Figure 2.

Figure 2. CRISPR/Cas9-mediated disruption of the *PEX* genes phenocopies the dysfunction of cholesterol trafficking to ciliary membranes.

A Western blot analysis showing the depletion of PEX1 and PEX14 and the normal processing of Shh protein in the $PEX1^{-/-}$ and $PEX14^{-/-}$ hTERT-RPE1 cell clones. GAPDH served as a loading control.

B Immunostaining with anti-PEX1 (red) or PEX14 (red), anti-PMP70 (green), anti-ninein (blue), and anti-acetylated-tubulin (white) in wild-type, $PEX1^{-/-}$, and $PEX14^{-/-}$ hTERT-RPE1 cells in quiescent G_0 phase. Arrowheads indicate primary cilia. Scale bar, 10 μm.

C Quantification of the number of PMP70-positive peroxisomes per cell from (B). Peroxisome formation in $PEX1^{-/-}$ and $PEX14^{-/-}$ hTERT-RPE1 cells was significantly impaired compared with that of the parental cells (mean ± s.d.: ***$P < 0.001$: one-way ANOVA with Tukey's HSD, $n = 3$: 20–25 cells per experiment).

D Quantification of proportion of ciliated cells from (B). Ciliogenesis in $PEX1^{-/-}$ and $PEX14^{-/-}$ hTERT-RPE1 cells was not significantly altered compared with that of the parental cells (mean ± s.d.: one-way ANOVA with Tukey's HSD, $n = 3$: 190–200 cells per experiment).

E Quiescent G_0-phase wild-type, $PEX1^{-/-}$, and $PEX14^{-/-}$ hTERT-RPE1 cells transfected with AcGFP1-tagged D4 as a cholesterol probe were immunostained with anti-pericentrin (white) and anti-acetylated-tubulin (blue) antibodies. Cholesterol was stained with Filipin III (red). Arrows and arrowheads indicate primary cilia and cytosolic accumulations of AcGFP1-tagged D4, respectively. Scale bar, 5 μm.

F Quantification of the Filipin III intensity at primary cilia from (E). $PEX1^{-/-}$ and $PEX14^{-/-}$ hTERT-RPE1 cells had significant reductions in the ciliary signal of Filipin III (***$P < 0.001$: one-way ANOVA with Tukey's HSD, $n = 3$: 40–50 cells per experiment). In the boxplot, medians, $25^{th}/75^{th}$ percentile, and min/max were represented by the central lines, the box limits, and the whiskers/error bars, respectively.

G Quantification of the AcGFP1-tagged D4 intensity at primary cilia from (E). The ciliary signal of AcGFP1-tagged D4 in $PEX1^{-/-}$ and $PEX14^{-/-}$ hTERT-RPE1 cells was significantly diminished (***$P < 0.001$: one-way ANOVA with Tukey's HSD, $n = 3$: 25–30 cells per experiment). In the boxplot, medians, $25^{th}/75^{th}$ percentile, and min/max were represented by the central lines, the box limits, and the whiskers/error bars, respectively.

H Quiescent G_0-phase wild-type, $PEX1^{-/-}$, and $PEX14^{-/-}$ hTERT-RPE1 cells were treated with or without 1.5% methyl-β-cyclodextrin for 45 min and then incubated with or without cholesterol (cholesterol/methyl-β-cyclodextrin complex) for 1 h. After removing exogenous cholesterol, they were stimulated with 50 nM Shh-N for 24 h in the presence of pravastatin, and then immunostained with anti-Smo (green), anti-acetylated-tubulin (blue), and anti-γ-tubulin (red) antibodies. For the alternative cholesterol complementation, LDL (0.06 mg/ml) was co-incubated with Shh-N and pravastatin for 24 h after methyl-β-cyclodextrin-mediated cholesterol depletion. Scale bar, 2.5 μm.

I Quantification of the Smo intensity at primary cilia in wild-type, $PEX1^{-/-}$, and $PEX14^{-/-}$ hTERT-RPE1 cells from (H). $PEX1^{-/-}$ and $PEX14^{-/-}$ hTERT-RPE1 cells exhibited the dampened Shh-N ligand-induced ciliary accumulation of Smo. The complementation of exogenous cholesterol (cholesterol/methyl-β-cyclodextrin complex) restored the ciliary accumulation of Smo in both *PEX*-knockout cells, while the LDL complementation did not rescue the ciliary phenotypes efficiently (*$P < 0.05$, **$P < 0.01$, ***$P < 0.001$: one-way ANOVA with Tukey's HSD, $n = 3$: 90–100 cells per experiment). In the boxplot, medians, $25^{th}/75^{th}$ percentile, and min/max were represented by the central lines, the box limits, and the whiskers/error bars, respectively.

Source data are available online for this figure.

Since EHD1 and EHD3, which belong to the EPS15 homology domain family involved in endosomal membrane trafficking, localize to the ciliary pocket membrane (Lu *et al*, 2015), we investigated their role in the contact between peroxisomes and primary cilia. The peroxisomal signals of PMP70 overlapped with the AcGFP1-tagged EHD3 signal in the ciliary pocket of hTERT-RPE1 cells (Fig 3F), suggesting that EHD1 and EHD3 are involved in the contact between peroxisomes and primary cilia. To verify this, we investigated the biochemical interaction between EHD1 or EHD3 and PEX14. Immunoprecipitation analysis and GST pull-down analysis demonstrated that EHD1 and EHD3 physically interact with PEX14 (Fig 3G and H). Three-dimensional constitution analysis of confocal images also revealed that the cholesterol-containing peroxisomes localized at the ciliary pocket labeled with AcGFP1-tagged EHD3 in the hTERT-RPE1 cells (Fig 3I). Next, we generated $EHD1^{-/-}$ and $EHD3^{-/-}$ hTERT-RPE1 cell clones using the CRISPR-ObLiGaRe method (Appendix Fig S6A–D, Appendix Tables S1 and S2). They showed lower levels of cholesterol in the ciliary membranes than wild-type hTERT-RPE1 cells (Appendix Fig S6E and F, Appendix Fig S2F and G). Although the $EHD1^{-/-}$ and $EHD3^{-/-}$ hTERT-RPE1 cells showed the contact times between peroxisomes and cilia, they exhibited significantly shorter duration of contact compared with the parental hTERT-RPE1 cells (Appendix Fig S7A–C, Movie EV5–EV7). We thus concluded that EHD1 and EHD3 are involved in the contact between peroxisomes and primary cilia.

ORP3 controls the cholesterol trafficking at the peroxisome–primary cilium contact site

Since ORP3, an OSH/ORP (oxysterol binding homology protein/ OSBP-related protein) protein family member involved in intracellular cholesterol trafficking, was detected in several sets of ciliary proteome data published previously (Fig 5A; Ishikawa *et al*, 2012; Kohli *et al*, 2017), we focused on the ORP3 molecule as a candidate lipid transfer protein underlying ciliary cholesterol trafficking. To test whether ORP3 is indeed involved in the supply of cholesterol into the primary cilia, we depleted the *ORP3* gene in hTERT-RPE1 cells using the CRISPR-ObLiGaRe method (Fig 5B, Appendix Tables S1 and S2). The $ORP3^{-/-}$ hTERT-RPE1 cell clones exhibited a lower level of cholesterol in the ciliary membranes even with a more significant increase of intracellular cholesterol levels than those of the parental hTERT-RPE1 cells (Fig 5C and D, Appendix Fig S2F and G, Appendix Fig S7D and E). They did not exhibit altered dynamic contact numbers between peroxisomes and cilia, but there was significant shortening of the duration of contact compared with that of the parental hTERT-RPE1 cells (Appendix Fig S7F–H, Movies EV8 and EV9), implying that ORP3 might prolong the half-life of contact between peroxisomes and primary cilia to mediate ciliary cholesterol trafficking.

To precisely determine the localization of ORP3 in the primary cilia, we stained endogenous ORP3 in the G_0-quiescent hTERT-RPE1 cells with anti-ORP3 antibody. The ORP3 signals were detected at the ciliary pocket and overlapped with the peroxisomal PMP70 signals of wild-type hTERT-RPE1 cells (Fig 5E). Consistent with the time-lapse imaging data, the PMP-70-positive signals merging with the phosphor-Ser473 Akt signal at the ciliary pocket significantly decreased in the $ORP3^{-/-}$ hTERT-RPE1 cells (Fig 5E and F), suggesting that the ORP3 molecule is a regulator of ciliary cholesterol trafficking at the peroxisome–primary cilium contact site. Analysis of the deletion mutant of ORP3 in the $ORP3^{-/-}$ hTERT-RPE1 cells revealed that the pleckstrin homology (PH) domain was required for the ciliary pocket localization for ciliary cholesterol trafficking (Fig 5H and I). Notably, the ORP3 mutants with deletion of the FFAT motif, which specifically interacts with the vesicle-associated
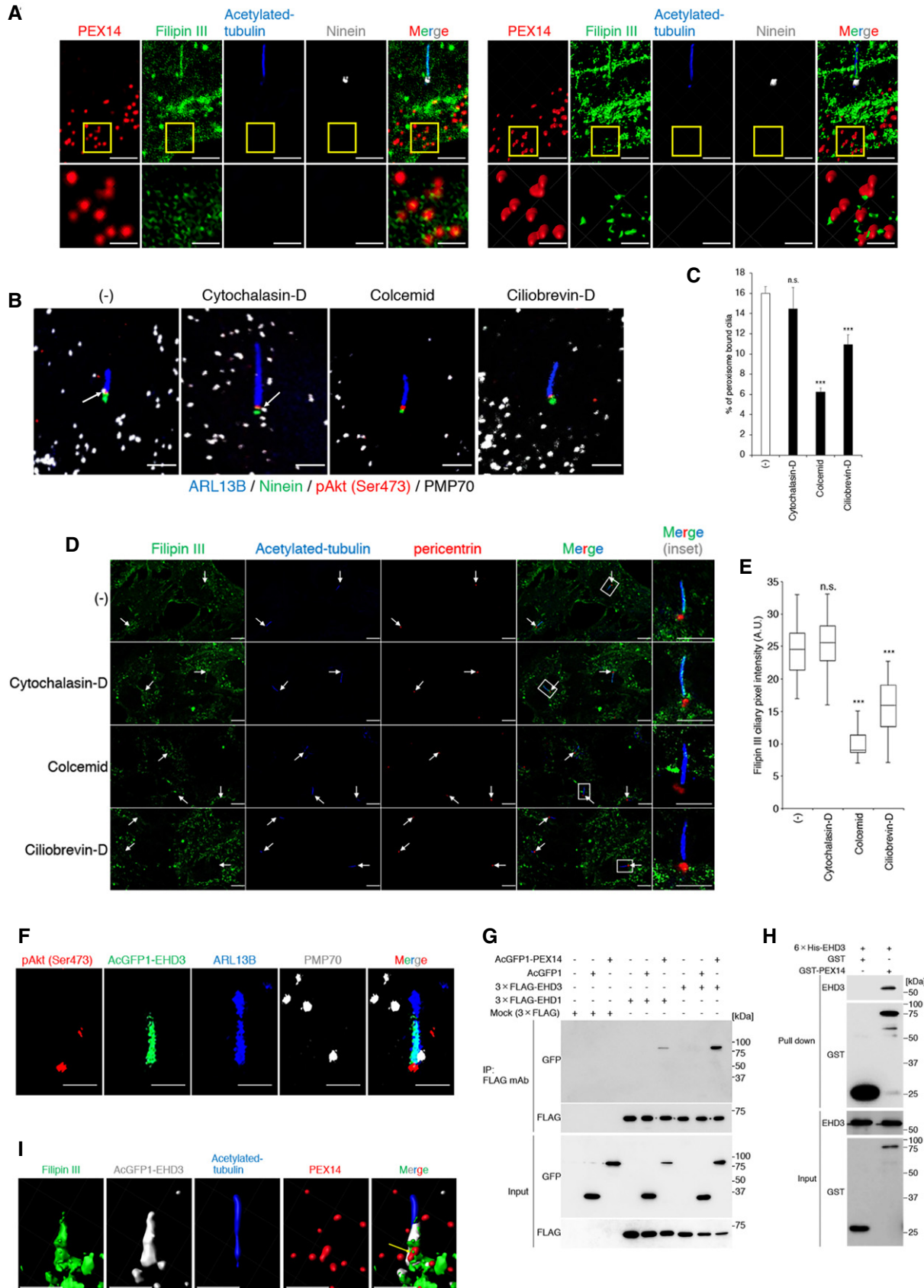
Figure 3.

Figure 3. Peroxisomes accompanied by cholesterol move along the microtubules to interact with the ciliary pocket structure.

A   Quiescent G_0-phase hTERT-RPE1 cells were immunostained with anti-PEX14 (red), anti-ninein (white), and anti-acetylated-tubulin (blue) antibodies. Cholesterol was stained with Filipin III (Green). Magnified images of the boxed regions showing peroxisome accompanied by cholesterol (arrows). Three-dimensional reconstitution of the same cell indicates that Filipin III stains the membrane regions of ciliary axonemes and peroxisomes. The scale bars indicate 2.5 μm and 1.25 μm in lower- and higher-magnified images, respectively.

B   Quiescent G_0-phase wild-type hTERT-RPE1 cells treated with Cytochalasin-D (200 nM), colcemid (50 nM), or Ciliobrevin-D (10 μM) for 6 h were immunostained with anti-ARL13B (blue), anti-phospho-S473-Akt (red), anti-ninein (green), and anti-PMP70 (white) antibodies. Arrows indicate the peroxisomes interacting with the ciliary pocket. Scale bar, 5 μm.

C   Quantification of proportion of primary cilia interacting with peroxisomes from (B). Colcemid (50 nM) and Ciliobrevin-D (10 μM) significantly inhibited the spatial interaction between peroxisomes and primary cilia (mean ± s.d.: ***$P < 0.001$: one-way ANOVA with Tukey's HSD, $n = 3$: 45–50 cells per experiment).

D   Quiescent G_0-phase wild-type hTERT-RPE1 cells were treated with Cytochalasin-D (200 nM), Colcemid (50 nM), or Ciliobrevin-D (10 μM) for 6 h and then immunostained with anti-acetylated-tubulin (blue) and anti-pericentrin (green) antibodies. Cholesterol was stained with Filipin III (green). Arrows indicate primary cilia. Scale bar, 2.5 μm.

E   Quantification of the Filipin III intensity at primary cilia from (D). Colcemid and Ciliobrevin-D interfered with the distribution of cholesterol in the ciliary membrane (***$P < 0.001$: one-way ANOVA with Tukey's HSD, $n = 3$: 40–50 cells per experiment). In the boxplot, medians, $25^{th}/75^{th}$ percentile, and min/max were represented by the central lines, the box limits, and the whiskers/error bars, respectively.

F   hTERT-RPE1 cells were transfected with AcGFP1-tagged EHD3 and cultured without serum for 24 h before immunostaining with anti-GFP (green), anti-ARL13B (blue), anti-PMP70 (white), and anti-phospho-S473-Akt (red) antibodies. The scale bars represent 2.5 μm.

G   3×FLAG-tagged EHD1 or EHD3 and AcGFP1-tagged PEX14 were coexpressed in HEK293T cells and then immunoprecipitated from whole-cell lysates using the anti-FLAG antibody. AcGFP1-tagged PEX14 and 3×FLAG-tagged EHD1 or EHD3 fragments in the IP fractions and inputs were detected by Western blotting.

H   Recombinant GST (0.2 μg) or GST fused to PEX14 proteins (1 μg) and 6×His-EHD3 protein (1 μg) were pulled down using glutathione-Sepharose beads. GST-tagged PEX14 and 6×His-tagged EHD3 proteins in the pull-down fractions and inputs were detected by western blotting.

I   3D reconstitution of the quiescent G_0-phase hTERT-RPE1 cells transfected with AcGFP1-tagged EHD3 (white) immunostained with anti-acetylated-tubulin (blue) and anti-PEX14 (red) antibodies. Cholesterol was stained with Filipin III (green). Cholesterol-containing peroxisome interacted with the ciliary pocket (arrow). The scale bars indicate 2 μm.

Source data are available online for this figure.

membrane protein-associated A/B (VAP-A/B), and the OSBP-homology domain (OHD), localized to the ciliary pocket, but they did not restore the defect in ciliary cholesterol in the $ORP3^{-/-}$ hTERT-RPE1 cells (Fig 5H and I), suggesting that the FFAT motif and OHD of ORP3 were indispensable for cholesterol trafficking at the ciliary pocket. To investigate the physical communication between peroxisome and primary cilia, we examined the biochemical interaction between ORP3 and PEX14, EHD1, or EHD3. Immunoprecipitation analysis demonstrated that ORP3 physically binds to PEX14 and EHD1 (Fig 5G). Indeed, the duration in which peroxisomes lingered at the AcGFP1-tagged EHD1-labeled ciliary pocket in $ORP3^{-/-}$ and $EHD3^{-/-}$hTERT-RPE1 cells was significantly shortened (Appendix Fig S8, Movie EV10–EV12). These findings revealed that ORP3 mediates the formation of peroxisome–primary cilium contact to control the cholesterol trafficking into the ciliary membrane.

The Rabin8 and Rab10 axis is required for the peroxisome dynamics for ciliary cholesterol trafficking

Rabin8, the specific GTP exchange factor (GEF) for the Rab8 GTPase family, has been implicated in both ciliogenesis (Nachury *et al*, 2007) and cholesterol trafficking to the PM (Kanerva *et al*, 2013). Thus, we focused on the Rabin8 molecule as a candidate regulator of peroxisome-mediated cholesterol trafficking to the ciliary membrane. Specifically, we depleted the *Rabin8* gene in hTERT-RPE1 cells using the CRISPR-ObLiGaRe method (Appendix Tables S1 and S2). Western blot analysis confirmed that there were no Rabin8 products in the $Rabin8^{-/-}$ hTERT-RPE1 cell clones (Appendix Fig S9A). Notably, ciliogenesis was not completely deficient in the $Rabin8^{-/-}$ hTERT-RPE1 cells (Appendix Fig S9B and C), implying that these knockout cell clones could be used for subsequent studies focusing on the dysfunction of ciliary cholesterol. As expected, depletion of the *Rabin8* gene significantly diminished the ciliary cholesterol levels compared with that in the parental

hTERT-RPE1 cells (Fig 6A and B, Appendix Fig S2F and G). The $Rabin8^{-/-}$ hTERT-RPE1 cells also showed defects in peroxisome dynamics and the subsequent contact between peroxisomes and primary cilia (Appendix Fig S9D–F, Movie EV13 and EV14, Fig 6C and D), suggesting that Rabin8 is involved in the peroxisome-mediated trafficking of cholesterol to the ciliary membrane. In contrast, $ABCD1^{-/-}$ and $NPC1^{-/-}$ hTERT-RPE1 cells generated by the CRISPR-ObLiGaRe method as a nonciliopathic but intracellular cholesterol accumulation disease model (X-ALD and NPC) did not alter the ciliary cholesterol level and dynamic contact between peroxisomes and primary cilia (Appendix Fig S10, Appendix Fig S2F and G, Movies EV15 and EV16).

Next, we sought to clarify whether the ciliary cholesterol insufficiency in the $Rabin8^{-/-}$ hTERT-RPE1 cells is a direct and specific result of losing the physical communication between peroxisomes and primary cilia using an inducible FRB-FKBP hetero-dimerization system. Application of the chemical inducer rapamycin enables coupling of the peroxisomes labeled with PEX3-GFP-FRB to the Bicaudal-D2 (BicD2) molecule, which is a subunit of the dynein motor complex involved in microtubule minus-end-directed organelle transport, fused with a fluorescent protein tdTomato and FKBP, thereby targeting the peroxisomes to the ciliary pocket rapidly and efficiently (Fig 6E and F, Movie EV17). Rapamycin treatment in the $Rabin8^{-/-}$ hTERT-RPE1 cells co-expressing PEX3-GFP-FRB and tdTomato-BicD2-FKBP restored the reduced ciliary cholesterol to the level in the parental hTERT-RPE1 cells (Fig 6G and H), indicating that the peroxisome is a direct source of the ciliary membrane cholesterol. These results suggest that the peroxisome-associated phenotypes in $Rabin8^{-/-}$ hTERT-RPE1 cells are correlated with ciliary dysfunction. Consistent with insufficient ciliary cholesterol in the $Rabin8^{-/-}$ hTERT-RPE1 cells, they exhibited significantly impaired ciliary localization of Smo following the Shh-N stimulation (Appendix Fig S9G and H), suggesting that the *Rabin8* gene is required for the Shh signal transduction. Notably, exogenous cholesterol (cholesterol/methyl-β-cyclodextrin complex), but not
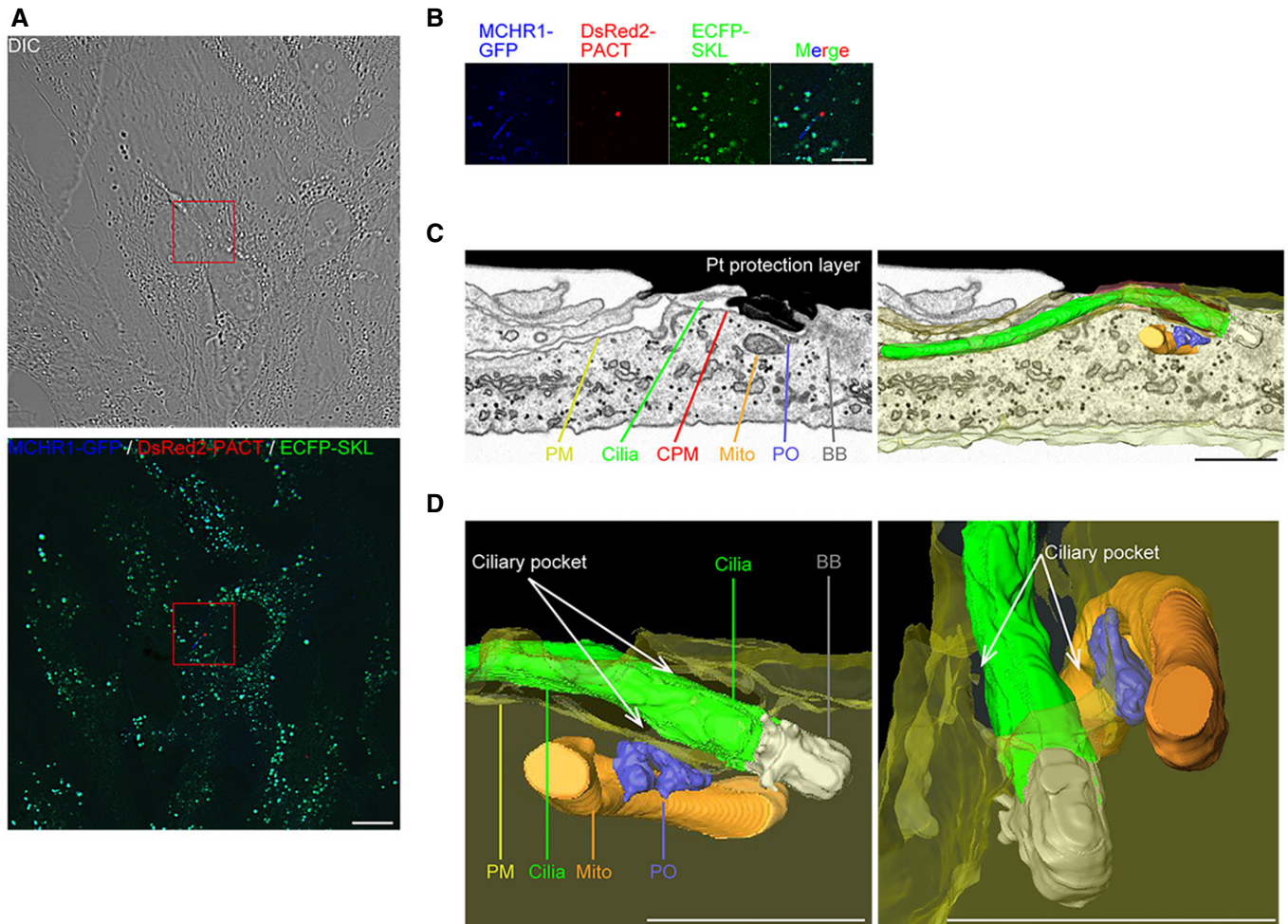
Figure 4. Three-dimensional analysis of interaction between the peroxisome and the ciliary pocket.

A   Maximum projection of z-stack sections of hTERT-RPE1 cells expressing MCHR1-GFP (blue), DsRed2-PACT (red), and ECFP-SKL (green) 48 h after serum starvation. The ECFP-SKL-positive cell with primary cilia, indicated by the red box, was analyzed by FIB-SEM. Top, differential interference contrast (DIC); bottom, merged image. Scale bar, 10 μm.

B   The fluorescent image of primary cilia, enlarged the area boxed in red in panel (A). Arrow indicates the ECFP-SKL-positive peroxisome associated with primary cilium. Scale bar, 5 μm.

C   Single FIB-SEM image (left) showing a cross section the ciliary pocket membrane, and 3D surface model reconstructed from segmented FIB-SEM images (right). Region of interest was coated by a protection layer of platinum before FIB milling. Plasma membrane (PM), yellow (surface view 75% transmission); cilia, green (surface view); ciliary pocket membrane (CPM), red (surface view 70% transmission); mitochondria (Mito), orange (surface view); peroxisome (PO), purple (surface view); basal body (BB), white (surface view). Scale bar, 1 μm.

D   Enlarged 3D view of peroxisome interacting with ciliary pocket and mitochondria. Left, x-y view; right, oblique view. Scale bar, 1 μm.

LDL, effectively restored the Shh-N-mediated accumulation of Smo in the *Rabin8*$^{-/-}$ hTERT-RPE1 cells (Appendix Fig S9G and H), implying that their ciliary dysfunction is attributable to insufficient ciliary cholesterol.

To identify the effector molecule of Rabin8 in the context of peroxisome-mediated ciliary cholesterol trafficking, we introduced Rab8 family members including Rab8A, Rab8B, and Rab10 and their constitutively active forms (Rab8A-Q67L, Rab8B-Q67L, and Rab10-Q68L; Nachury *et al*, 2007; Homma & Fukuda, 2016) tagged with AcGFP1 or GFP into the *Rabin8*$^{-/-}$ hTERT-RPE1 cells. We found that only AcGFP1-tagged Rab10-Q68L mutant effectively restored the accumulation of ciliary cholesterol to a level similar to that of AcGFP1-tagged Rabin8 in the *Rabin8*$^{-/-}$ hTERT-RPE1 cells (Fig 6I

and J). Notably, it was reported that Rab10 localizes to peroxisomes in mammalian cells (Gronemeyer *et al*, 2013). Confocal images revealed that the Rabin8- and Rab10-bound peroxisomes localized near the ciliary pocket labeled with AcGFP1-tagged EHD3 in the hTERT-RPE1 cells (Appendix Fig S9I, Appendix Fig S11G). GST-pull-down assay also demonstrated that both Rabin8 and Rab10 directly bind to PEX14 (Appendix Fig S9J, Appendix Fig S11H). These findings suggest that Rab10 functions as a main effector of Rabin8 in the context of ciliary cholesterol trafficking. Disruption of the *Rab10* gene in hTERT-RPE1 cells by the CRISPR-ObLiGaRe method also significantly decreased ciliary cholesterol and the dynamic contacts between peroxisomes and primary cilia (Appendix Tables S1 and S2, Appendix Fig S2F and G, Appendix Fig
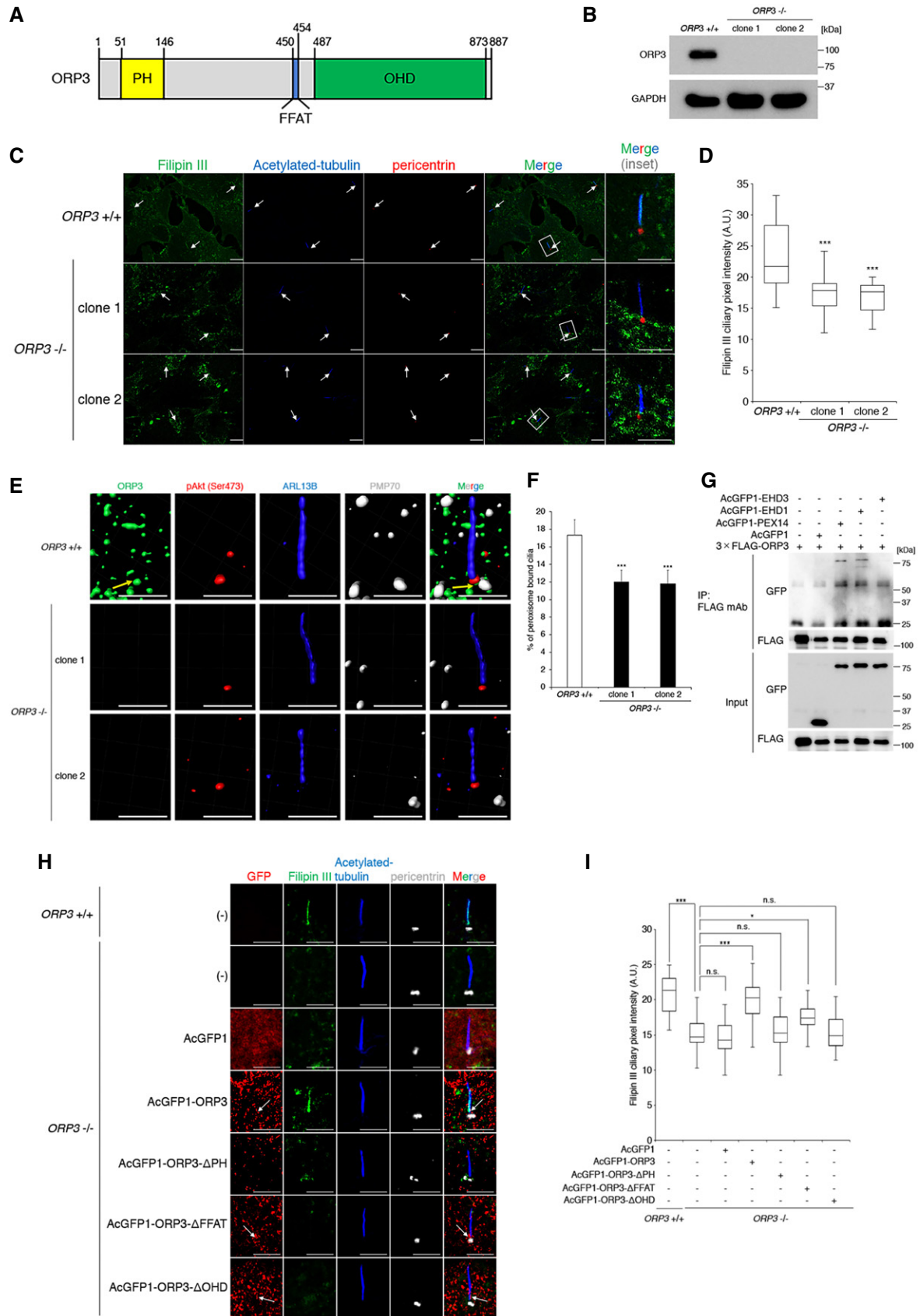
Figure 5.

Figure 5.   ORP3 is involved in the peroxisome-mediated cholesterol supply into the ciliary membrane.

A   Schematic of ORP3 structure. ORP3 contains an N-terminal pleckstrin homology (PH) domain that interacts with phospholipids, an FFAT motif that specifically interacts with VAP-A/B, and a highly conserved C-terminal OSBP-homology domain (OHD).

B   Western blot analysis showing depletion of ORP3 in the $ORP3^{-/-}$ hTERT-RPE1 cell clones. GAPDH served as a loading control.

C $ORP3^{+/+}$ and $ORP3^{-/-}$ hTERT-RPE1 cells incubated for 24 h without serum were immunostained with anti-pericentrin (red) and anti-acetylated-tubulin (blue) antibodies. Cholesterol was stained with Filipin III (green). Arrows indicate primary cilia. Scale bar, 5 μm.

D   Quantification of the Filipin III intensity at primary cilia from (C). $ORP3^{-/-}$ hTERT-RPE1 cells exhibited a significant reduction of ciliary cholesterol (***$P < 0.001$: one-way ANOVA with Tukey's HSD, $n = 3$: 40–50 cells per experiment). In the boxplot, medians, 25th/75th percentile, and min/max were represented by the central lines, the box limits, and the whiskers/error bars, respectively.

E   Three-dimensional reconstitution of the quiescent G_0-phase $ORP3^{+/+}$ and $ORP3^{-/-}$ hTERT-RPE1 cells immunostained with anti-ARL13B (blue), anti-phospho-S473-Akt (red), anti-ORP3 (green), and anti-PMP70 (white) antibodies indicates that ORP3 at the ciliary pocket (arrow and arrowhead) mediates the membrane regions of ciliary pocket and peroxisomes (arrowhead). The scale bars indicate 5 μm.

F   Quantification of proportion of primary cilia interacting with peroxisomes from (E). Depletion of $ORP3$ significantly interfered with the spatial interaction between peroxisomes and primary cilia (mean ± s.d.: ***$P < 0.001$: one-way ANOVA with Tukey's HSD, $n = 3$: 45–50 cells per experiment).

G   3×FLAG-tagged ORP3 and AcGFP1-tagged PEX14, EHD1, or EHD3 were coexpressed in HEK293T cells and then immunoprecipitated from whole-cell lysates using the anti-FLAG antibody. 3×FLAG-tagged ORP3 and AcGFP1-tagged PEX14, EHD1 or EHD3 fragments in the IP fractions and inputs were detected by Western blotting.

H $ORP3^{-/-}$ hTERT-RPE1 cells were transfected with AcGFP1-tagged ORP3, PH domain-deleted-ORP3 mutant (ΔPH), FFAT motif-deleted-ORP3 mutant (ΔFFAT), or OHD domain-deleted-ORP3 mutant (ΔOHD) and cultured without serum for 24 h before Filipin III (green)-mediated cholesterol staining and immunostaining with anti-GFP (red), anti-pericentrin (white), and anti-acetylated-tubulin (blue) antibodies. Arrows represent AcGFP1-tagged ORP3 or the mutants localized to the ciliary pocket. AcGFP1-tagged ORP3ΔPH mutant mis-localized to the ciliary pocket. The scale bars indicate 5 μm.

I   Quantification of the Filipin III intensity at primary cilia from (H). AcGFP1-tagged ORP3 deletion mutants did not restore the ciliary cholesterol insufficiency in the $ORP3^{-/-}$ hTERT-RPE1 cells (*$P < 0.05$, ***$P < 0.001$: one-way ANOVA with Tukey's HSD, $n = 3$: 40–50 cells per experiment). In the boxplot, medians, 25th/75th percentile, and min/max were represented by the central lines, the box limits, and the whiskers/error bars, respectively.

Source data are available online for this figure.

S11A–F, Movie EV18 and EV19), indicating that Rab10 is required for peroxisome-mediated ciliary cholesterol trafficking. These findings suggest that the Rabin8–Rab10 cascade controls the dynamics of peroxisomes for ciliary cholesterol trafficking.

The PEX14–Rab10–KIFC3 complex drives peroxisome dynamics along the microtubules for ciliary cholesterol trafficking

A C-terminal kinesin molecule, KIFC3, involved in microtubule minus-end-directed organelle transport (Appendix Fig S12A) was

previously identified as a binding partner of PEX1 using a yeast two-hybrid screen (Dietrich *et al*, 2013). To study whether KIFC3 physically interacts with the peroxisomal membrane proteins, we investigated the biochemical interaction between KIFC3 and PEX14. Immunoprecipitation analysis with FLAG antibody in HEK293T cells transfected with 3×FLAG-tagged KIFC3 and AcGFP1-tagged PEX14 demonstrated the physical interaction between KIFC3 and PEX14 (Fig 7A), implying that peroxisomes associate with microtubules via KIFC3. The N-terminal region including the rod domain in KIFC3 is required for the interaction with PEX14 (Appendix Fig S12B). Next,

Figure 6.   Rabin8 cooperates with Rab10 to control the peroxisome-mediated supply of cholesterol to the ciliary membrane.

A $Rabin8^{+/+}$ and $Rabin8^{-/-}$ hTERT-RPE1 cells incubated for 24 h without serum were immunostained with anti-pericentrin (red) and anti-acetylated-tubulin (blue) antibodies. Cholesterol was stained with Filipin III (green). Scale bar, 5 μm.

B   Quantification of the Filipin III intensity at primary cilia from (A). $Rabin8^{-/-}$ hTERT-RPE1 cells exhibited a significant reduction of ciliary cholesterol (***$P < 0.001$: one-way ANOVA with Tukey's HSD, $n = 3$: 40–50 cells per experiment). In the boxplot, medians, 25th/75th percentile and min/max were represented by the central lines, the box limits, and the whiskers/error bars, respectively.

C   Quiescent G_0-phase $Rabin8^{+/+}$ and $Rabin8^{-/-}$ hTERT-RPE1 cells were immunostained with anti-ARL13B (blue), anti-phospho-S473-Akt (red), anti-ninein (green), and anti-PMP70 (white) antibodies. Arrow indicates the peroxisomes contacting the ciliary pocket. Scale bar, 5 μm.

D   Quantification of (C) indicating that disruption of the $Rabin8$ gene significantly inhibited the spatial interaction between peroxisomes and primary cilia (mean ± s.d.: ***$P < 0.001$: one-way ANOVA with Tukey's HSD, $n = 3$: 45–50 cells per experiment).

E   Schematic representation of the rapamycin-inducible peroxisome targeting to the ciliary pocket system.

F   Quiescent G_0-phase hTERT-RPE1 cells transiently expressing PEX3-GFP-FRB (green) and tdTomato-BicD2-FKBP (red) treated with rapamycin were imaged live for 10 min by confocal microscopy (Movie EV10). Scale bar, 5 μm.

G   Quiescent G_0-phase $Rabin8^{+/+}$ and $Rabin8^{-/-}$ hTERT-RPE1 cells transfected with PEX3-GFP-FRB (red) and tdTomato-BicD2-FKBP (white) were treated with or without 100 μM rapamycin for 30 min, and then immunostained with anti-acetylated-tubulin (blue) antibody. Cholesterol was stained with Filipin III (Green). Arrows indicate the enrichment of ciliary cholesterol. The scale bars represent 5 μm.

H   Quantification of the Filipin III intensity at primary cilia from (G). Rapamycin-induced peroxisome targeting to the ciliary pocket restored the reduction of ciliary cholesterol in the $Rabin8^{-/-}$ hTERT-RPE1 cells (***$P < 0.001$: one-way ANOVA with Tukey's HSD, $n = 3$: 40–50 cells per experiment). In the boxplot, medians, 25th/75th percentile, and min/max were represented by the central lines, the box limits, and the whiskers/error bars, respectively.

I $Rabin8^{-/-}$ hTERT-RPE1 cells were transfected with AcGFP1-tagged Rabin8, GFP-tagged Rab8A, GFP-tagged Rab8A-Q67L (constitutively active form), GFP-Rab8B, GFP-Rab8B-Q67L (constitutively active form), AcGFP1-tagged Rab10, or AcGFP1-tagged Rab10-Q68L (constitutively active form), and then immunostained with anti-GFP (red), anti-acetylated-tubulin (blue), and anti-ninein (white) antibodies. Cholesterol was stained with Filipin III (Green). Arrows indicate the enrichment of ciliary cholesterol. The scale bars represent 5 μm.

J   Quantification of (I) showing that AcGFP1-tagged Rabin8 and AcGFP1-tagged Rab10-Q68L effectively restored the defect in ciliary enrichment of cholesterol in $Rabin8^{-/-}$ hTERT-RPE1 cells (***$P < 0.001$: one-way ANOVA with Tukey's HSD, $n = 3$: 35–40 cells per experiment). In the boxplot, medians, 25th/75th percentile, and min/max were represented by the central lines, the box limits, and the whiskers/error bars, respectively.
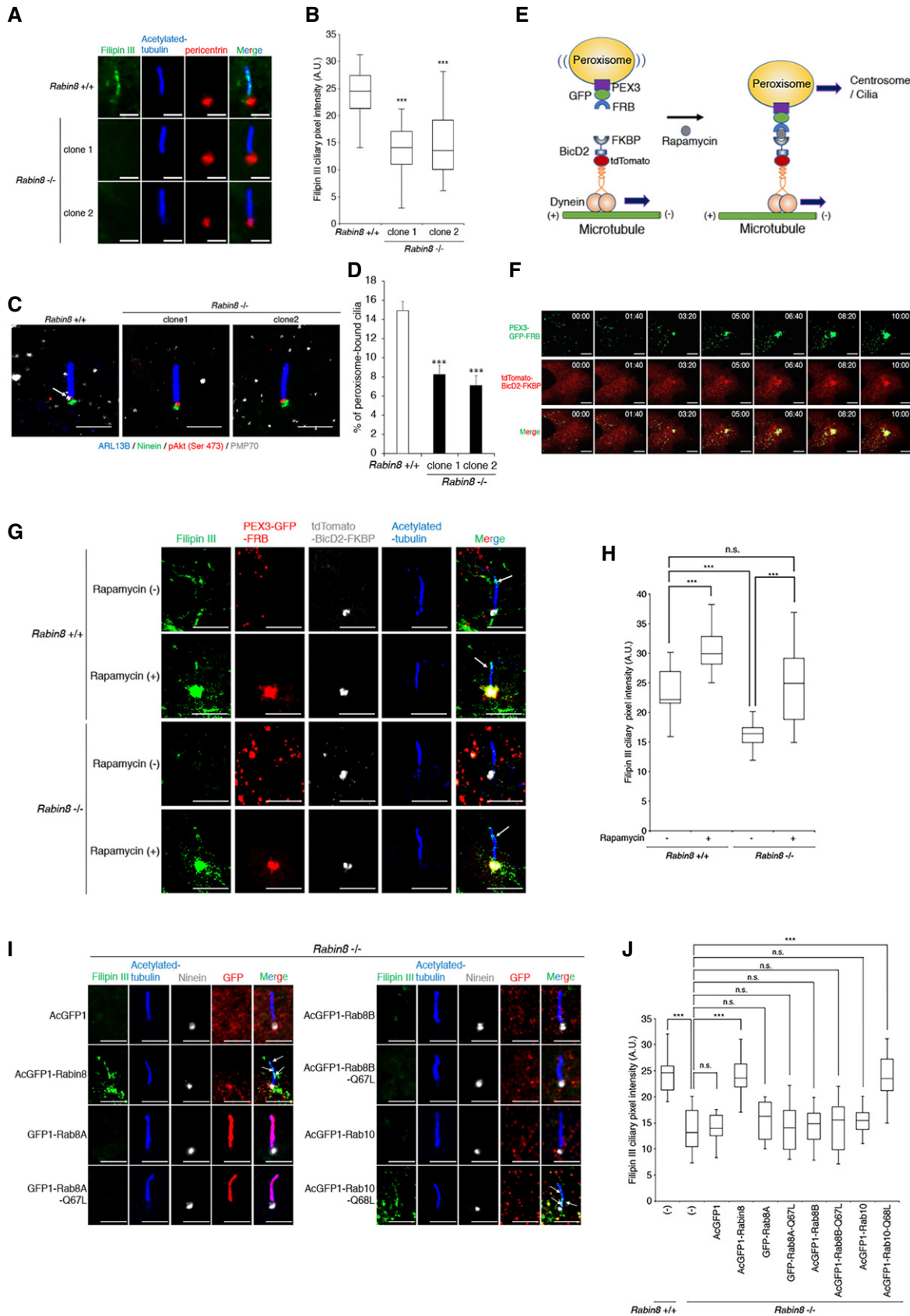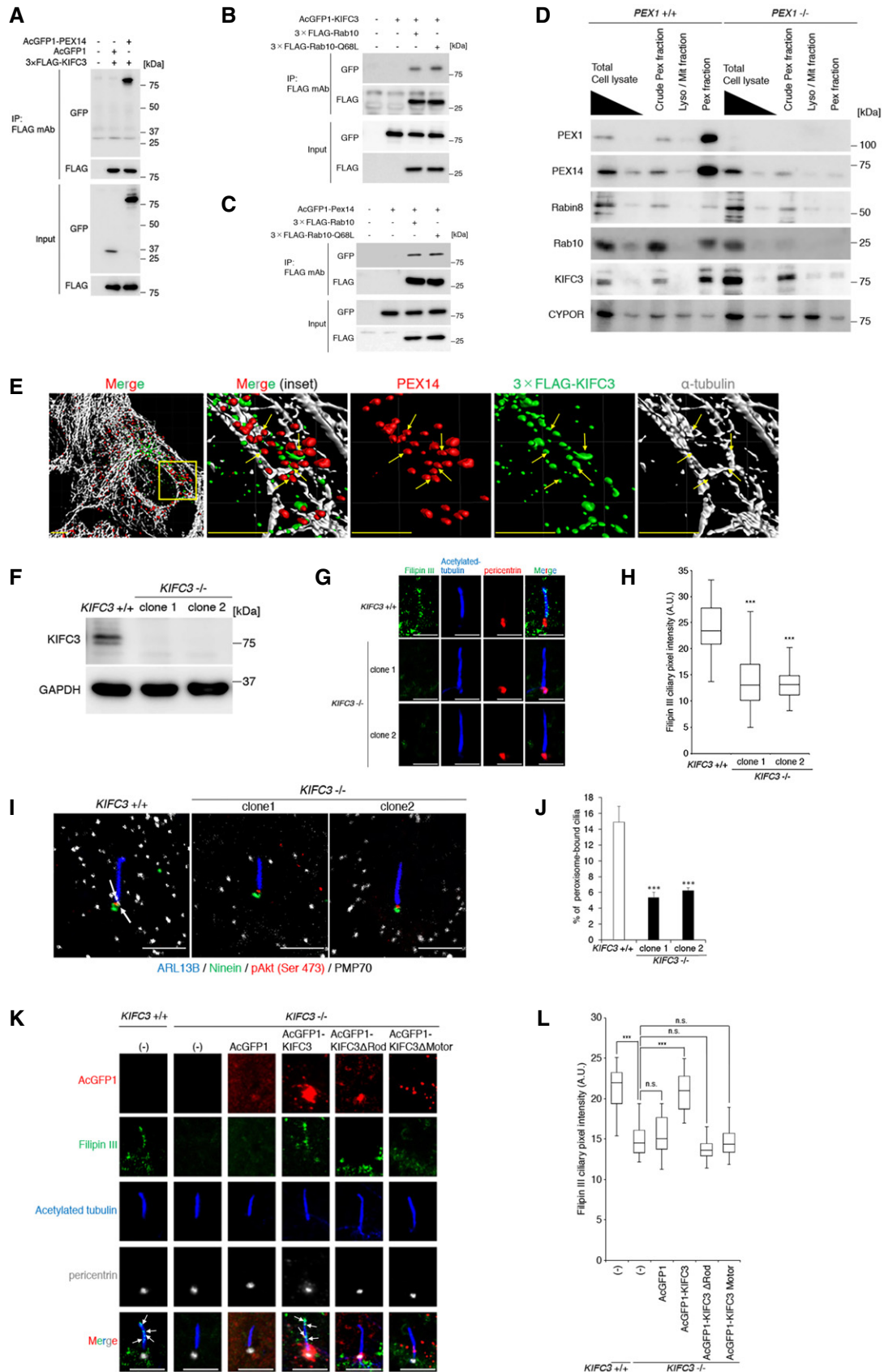
Figure 6.

Figure 7.

Figure 7. The Rabin8–Rab10–KIFC3 complex is implicated in the peroxisome-mediated supply of cholesterol into the ciliary membrane.

A Whole-cell lysates from HEK293T cells expressing AcGFP1 or AcGFP1-tagged PEX14 and 3×FLAG-tagged KIFC3 were immunoprecipitated with anti-FLAG antibody and immunoblotted with anti-GFP or anti-FLAG antibody.

B Whole-cell lysates from HEK293T cells expressing AcGFP1-tagged KIFC3 and 3×FLAG-tagged Rab10 or Rab10-Q68L were immunoprecipitated with anti-FLAG antibody and immunoblotted with anti-GFP or anti-FLAG antibody.

C Whole-cell lysates from HEK293T cells expressing AcGFP1-tagged Pex14 and 3×FLAG-tagged Rab10 or Rab10-Q68L were immunoprecipitated with anti-FLAG antibody and immunoblotted with anti-GFP or anti-FLAG antibody.

D Western blot analysis of the ciliary cholesterol trafficking-associated components in $Pex1^{+/+}$ and $Pex1^{-/-}$ hTERT-RPE1 cells. Total cell lysates were separated to crude peroxisomal (Crude Pex), lysosomal and mitochondrial (Lyso/Mito), and peroxisomal (PEX) fractions. CYPOR, a lysosomal and mitochondrial protein, served as a positive control for the Lyso/Mito fractionation. Total cell lysates were gradually injected at 20 μg and 5 μg into a gel for SDS–PAGE, while equal amounts (5 μg) of protein from each fraction were loaded. Rabin8, Rab10, and KIFC3 were concentrated in the PEX fraction in $Pex1^{+/+}$ hTERT-RPE1 cells. CYPOR (cytochrome P450 reductase) is a mitochondrial protein.

E Quiescent G_0-phase hTERT-RPE1 cells transfected with 3×FLAG-tagged KIFC3 were immunostained with anti-FLAG (green), anti-PEX14 (red), and anti-α-tubulin (white) antibodies. Magnified 3D-constituted images of the boxed regions showing peroxisomes are located on the microtubule arrays via KIFC3 (arrows). The scale bars indicate 5 μm.

F Western blot analysis showing depletion of KIFC3 in the $KIFC3^{-/-}$ hTERT-RPE1 cell clones. GAPDH served as a loading control.

G $KIFC3^{+/+}$ and $KIFC3^{-/-}$ hTERT-RPE1 cells incubated for 24 h without serum were immunostained with anti-pericentrin (red) and anti-acetylated-tubulin (blue) antibodies. Cholesterol was stained with Filipin III (green). Scale bar, 5 μm.

H Quantification of (G) indicating that $KIFC3^{-/-}$ hTERT-RPE1 cells significantly reduced the ciliary accumulation of cholesterol (***$P < 0.001$: one-way ANOVA with Tukey's HSD, $n = 3$: 40–50 cells per experiment). In the boxplot, medians, 25th/75th percentile, and min/max were represented by the central lines, the box limits, and the whiskers/error bars, respectively.

I Quiescent G_0-phase $KIFC3^{+/+}$ and $KIFC3^{-/-}$ hTERT-RPE1 cells were immunostained with anti-ARL13B (blue), anti-phospho-S473-Akt (red), anti-ninein (green), and anti-PMP70 (white) antibodies. Arrows represent the peroxisomes contacting the ciliary pocket. Scale bar, 5 μm.

J Quantification of (I) showing that disruption of the $KIFC3$ gene significantly interfered with the contact between peroxisomes and primary cilia (mean ± s.d.: ***$P < 0.001$: one-way ANOVA with Tukey's HSD, $n = 3$: 45–50 cells per experiment).

K $KIFC3^{-/-}$ hTERT-RPE1 cells were transfected with AcGFP1, AcGFP1-tagged KIFC3, rod domain-deleted KIFC3 mutant (ΔRod), or motor domain-deleted KIFC3 mutant (ΔMotor) and cultured without serum for 24 h before Filipin III (green)-mediated cholesterol staining and immunostaining with anti-GFP (red), anti-pericentrin (white), and anti-acetylated-tubulin (blue) antibodies. Arrows represent ciliary localization of cholesterol. The scale bars indicate 5 μm.

L Quantification of the Filipin III intensity at primary cilia from (K). AcGFP1-tagged KIFC3 deletion mutants did not restore the ciliary cholesterol insufficiency in the $KIFC3^{-/-}$ hTERT-RPE1 cells (mean ± s.d.: ***$P < 0.001$: one-way ANOVA with Tukey's HSD, $n = 3$: 40–50 cells per experiment). In the boxplot, medians, 25th/75th percentile, and min/max were represented by the central lines, the box limits, and the whiskers/error bars, respectively.

Source data are available online for this figure.

we tested the mutual physical interactions among KIFC3, PEX14, and Rab10 using immunoprecipitation analyses. KIFC3 also physically interacts with Rab10 in a manner dependent on kinesin motor domain (Fig 7B and Appendix Fig S12C), implying that KIFC3 might be a downstream effector of Rab10 for the peroxisome-mediated trafficking of ciliary cholesterol. Moreover, the physical interaction between Rab10 and PEX14 was also detected in immunoprecipitation analysis (Fig 7C), suggesting that PEX14, Rab10, and KIFC3 form a complex associated with peroxisomes. Peroxisomal fractionation of whole-cell lysates from $PEX1^{+/+}$ and $PEX1^{-/-}$ hTERT-RPE1 cells demonstrated that Rabin8, Rab10, and KIFC3 are concentrated in the PEX1- and PEX14-enriched fraction, suggesting that the Rab10–KIFC3 complex associates with peroxisomes (Fig 7D). To precisely determine the spatial relationship among peroxisomes, microtubules, and KIFC3, we stained them in serum-starved hTERT-RPE1 cells transfected with 3×FLAG-tagged KIFC3. Three-dimensional reconstitution analysis of confocal images revealed that the KIFC3 signals were present at the interface between α-tubulin signal-marked microtubules and PEX14 signal-labeled peroxisomes (Fig 7E). Time-lapse imaging demonstrated that the KIFC3-bound peroxisomes moved to centrosomes in a motor domain-dependent manner (Appendix Fig S12D and E, Movies EV21 and EV23), implying that KIFC3 loads peroxisomes on the microtubule networks to control the microtubule minus-end-directed transport of peroxisomes. In addition, the deleted KIFC3-Rod domain mutant moved to centrosomes, but did not associate with peroxisomes, thereby inhibiting the peroxisome-to-centrosome contact (Appendix Fig S12D and E, Movie EV22). These results suggest that the PEX14–Rab10–KIFC3 complex regulates the microtubule-dependent dynamics of peroxisomes for the trafficking of ciliary cholesterol.

To clarify whether the KIFC3 motor activity contributes to the peroxisome-mediated supply of cholesterol to the ciliary membrane, we disrupted the $KIFC3$ gene in hTERT-RPE1 cells using the CRISPR-ObLiGaRe method (Appendix Tables S1 and S2). Western blot analysis demonstrated no KIFC3 products in the knockout cell clones (Fig 7F). Depletion of the $KIFC3$ gene significantly reduced the ciliary Filipin III and AcGFP1-tagged D4 signals compared with those in the parental hTERT-RPE1 cells (Fig 7G and H, Appendix Fig S2F and G). The $KIFC3^{-/-}$ hTERT-RPE1 cells also showed defective peroxisome dynamics and insufficient contact between peroxisomes and primary cilia (Appendix Fig S11D–F, Fig 7I and J, Movie EV20). Analysis of the deletion mutants of KIFC3 in the $KIFC3^{-/-}$ hTERT-RPE1 cells revealed that both rod and motor domains were indispensable for ciliary cholesterol trafficking (Fig 7K and L), suggesting that the physiological dynamics of KIFC3-bound peroxisomes is required for ciliary cholesterol trafficking. Notably, the rapamycin-dependent targeting of peroxisomes to the ciliary pocket restored the insufficient ciliary cholesterol in the $KIFC3^{-/-}$ and $Rab10^{-/-}$ hTERT-RPE1 cells, but not in the $ORP3^{-/-}$ and $EHD3^{-/-}$ hTERT-RPE1 cells, to the level in the parental hTERT-RPE1 cells (Fig 8A and B), suggesting that the peroxisomal Rab10-KIFC3 complex and the ciliary pocket proteins EHD3 and ORP3 might ensure the peroxisome dynamics and the cholesterol transfer to the ciliary membrane, respectively. In addition, the peroxisomes targeted to the ciliary pocket using the FRB-FKBP system in $KIFC3^{-/-}$, $ORP3^{-/-}$, $EHD3^{-/-}$, and $Rab10^{-/-}$ hTERT-RPE1 cells showed the significant signal intensity of Filipin III (Fig 8A and B), implying that these gene products might be dispensable for the transport of cholesterol to peroxisomes. Based on these results, we propose a model where (i) peroxisomes with

cholesterol are attached to microtubule networks via the PEX14–Rab10–KIFC3 complex and (ii) the Rabin8–Rab10–KIFC3 activity directs peroxisomes to the microtubule minus end, enabling the communication of peroxisomes with the ciliary pocket via ORP3, EHD1, and EHD3 for the supply of cholesterol to the ciliary membrane (Fig 8C).

Discussion

Primary cilia composed of a core of axonemal microtubules overlain by a membrane sense extracellular signals via ciliary membrane receptors to control cell proliferation and differentiation. For cilia to signal sensitively, both the protein and the lipid compositions of their
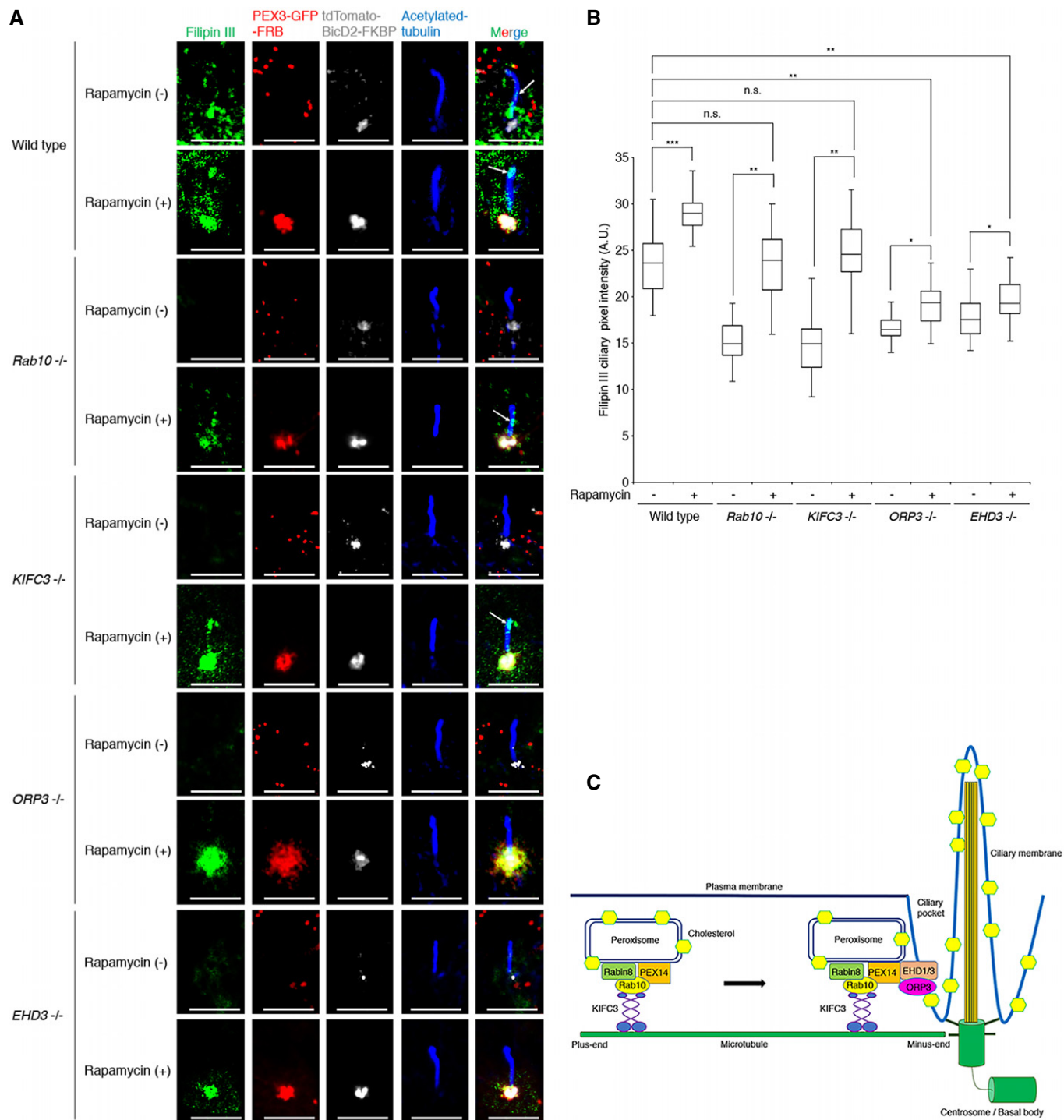

Figure 8.

Figure 8. Peroxisomes directly contribute to the cholesterol supply into ciliary membranes.

A Quiescent G₀-phase wild-type, *Rab10*$^{-/-}$, *KIFC3*$^{-/-}$, *ORP3*$^{-/-}$, and *EHD3*$^{-/-}$ hTERT-RPE1 cells transfected with PEX3-GFP-FRB (red) and tdTomato-BicD2-FKBP (white) were treated with or without 100 μM rapamycin for 30 min and then immunostained with anti-acetylated-tubulin (blue) antibody. Cholesterol was stained with Filipin III (Green). Arrows indicate the enrichment of ciliary cholesterol. The scale bars represent 5 μm.

B Quantification of the Filipin III intensity at primary cilia from (A). Rapamycin-induced peroxisome targeting to the ciliary pocket restored the insufficiency of ciliary cholesterol in the *Rab10*$^{-/-}$ and *KIFC3*$^{-/-}$ hTERT-RPE1 cells, but not in *ORP3*$^{-/-}$ and *EHD3*$^{-/-}$ hTERT-RPE1 cells (*$P < 0.05$, **$P < 0.01$, ***$P < 0.001$: one-way ANOVA with Tukey's HSD, $n = 3$: 35–40 cells per experiment). In the boxplot, medians, 25th/75th percentile, and min/max were represented by the central lines, the box limits, and the whiskers/error bars, respectively.

C Model for the molecular machinery for the supply of cholesterol into the ciliary membrane. The Rabin8–Rab10–KIFC3 complex associates peroxisomes with cholesterol to load them on microtubule arrays. KIFC3-mediated microtubule minus-end-directed movement guides peroxisomes to the ciliary pocket for the supply of cholesterol to the ciliary membrane. The ORP3–EHD1–EHD3 complex is involved in cholesterol trafficking at the ciliary pocket. In the pathological context of ZS, insufficient ciliary cholesterol might impair the cilium-related Shh signal competence, causing ciliopathy-related symptoms.

membranes must be compartmentalized from those of the PM (Garcia *et al*, 2018; Nachury, 2018). In mammalian cells, ciliary cholesterol is essential for Shh signaling, as both Ptch1 and Smo directly bind to cholesterol as a form of regulation in the shuttling from the ciliary membrane to other membranes (Corbit *et al*, 2005; Rohatgi *et al*, 2007; Byrne *et al*, 2016; Luchetti *et al*, 2016; Myers *et al*, 2017). Although it has been established that cells from NPC patients show the severe insufficiency of cholesterol in the PM (Kwon *et al*, 2009), most patients do not exhibit conditions on the ciliopathy clinical spectrum, implying the existence of specific routes of cholesterol to primary cilia. However, the mechanisms by which cellular cholesterol is trafficked into ciliary membranes are poorly understood. Here, we found that peroxisomes are necessary for the intracellular cholesterol trafficking into ciliary membranes, and that cells from ZS patients and *PEX*-knockout cell lines show defects in ciliary cholesterol localization and Shh signal transduction (Figs 1 and 2). Our findings suggest that the severe decrease in the number of peroxisomes as a carrier of cholesterol to primary cilia contributes to ciliopathy-associated symptoms including polycystic kidney and retinitis pigmentosa in ZS. In contrast, the MCH signal-dependent ciliary shortening was not impaired in the *PEX14*-knockout cells (Appendix Fig S2B and C), implying that all ciliary signaling pathways are not controlled by ciliary cholesterol. It was reported that siRNA-mediated knockdown of the *PEX1* or *PEX3* genes impaired ciliogenesis in RPE1 cells (Abe *et al*, 2017). However, the *PEX1*- and *PEX14*-knockout RPE1 cells and the ZS patient cells did not show any impairment of ciliogenesis (Fig 2D, Appendix Fig S1B). In a previous study, a knockdown assay using two independent siRNAs against the *PEX* genes was carried out, but the genetic complementation assay was not performed (Abe *et al*, 2017), implying that the possibility of the off-target effect of siRNA on ciliogenesis could not be completely ruled out. Another possible explanation for the phenotypic discrepancy of ciliogenesis among the *PEX*-knockout and knockdown cells is genetic compensation induced by deleterious mutations but not transcriptional or translational knockdown (Rossi *et al*, 2015). Peroxisome biogenesis disorders (PBDs) caused by germline mutations of *PEX* genes have genetic and pathogenic heterogeneity. PBDs are categorized into ZS, neonatal adrenoleukodystrophy (NALD), infantile Refsum disease (IRD), and rhizomelic chondrodysplasia punctata (RCDP) according to the clinical features (Fujiki, 2016). In general, the syndromes other than ZS, which is the most severe across the lifespan, are not accompanied by polycystic kidney, a hallmark symptom of ciliopathy. It remains unclear which factors determine whether the ciliopathy-associated features appear in PBDs. Further comparative studies of all PBD patient cells or disease model cells/animals will be required to clarify this.

In addition to PBDs, congenital peroxisomal diseases include many single-enzyme deficiencies. Of these, X-ALD is a neurodegenerative but nonciliopathic disorder caused by germline mutations of the *ABCD1* gene encoding an ATP-binding cassette (ABC) transporter, ABCD1, involved in the transport of long-chain and very long-chain fatty acids or their CoA derivatives into the peroxisomal matrix for lipid metabolism (Mosser *et al*, 1993). Since the issue of whether peroxisomal lipid metabolism is involved in ciliary functions is important for understanding the pathological mechanisms underlying ciliopathies, X-ALD is a suitable target disease for study. Consistent with a previous report (Chu *et al*, 2015), we here also observed the profound intracellular accumulation of cholesterol in patients' cells (Appendix Fig S1F), suggesting that ABCD1 is involved in intracellular cholesterol trafficking. However, the patients' cells and *ABCD1*-knockout cells showed a normal distribution of ciliary cholesterol and Shh signal response (Fig 1A–E, Appendix Fig S1C and Appendix Fig S10). Notably, disruption of the *ABCD1* gene did not alter the number of peroxisomes (Chang *et al*, 1999), indicating that ABCD1 is dispensable for peroxisome biogenesis. These findings imply that peroxisomes are essential for ciliary cholesterol trafficking. Since many peroxisomal single-enzyme deficiencies have been reported (Wanders, 2014; Argyriou *et al*, 2016; Fujiki, 2016), it has remained unclear whether defects in peroxisomal metabolic activities contribute to ciliopathies, the clarification of which requires further studies.

How do peroxisomes communicate with primary cilia in the context of cholesterol trafficking? Here, we demonstrate that peroxisomes move along the microtubules to interact with primary cilia. It was previously reported that LDL-derived cholesterol after NPC1/NPC2-dependent egress is trafficked to the PM via a Rab8A–myosin5B–actin-dependent membrane transport system (Kanerva *et al*, 2013). In contrast, our inhibitor analyses revealed that the peroxisome dynamics to primary cilia is not dependent on actin filaments (Fig 3B and C, Appendix Fig S4), suggesting the peroxisome-mediated cholesterol trafficking to primary cilia is clearly distinct from the route of actin-mediated cholesterol trafficking to the PM. We also here used a reverse genetics screen of the candidate genes to indicate that the microtubule minus-end-directed movement of peroxisomes is driven by the Rabin8–Rab10–KIFC3 complex. Since the ciliary membrane and the plasma membrane are contiguous in the cell, it is difficult to clarify whether the peroxisomes controlled by the Rabin8–Rab10–KIFC3 complex deliver cholesterol into the ciliary membrane directly or indirectly through the other plasma membrane. Rapamycin-induced targeting of peroxisomes to the ciliary pocket enabled the delivery of ciliary cholesterol even in the *Rabin8-*, *Rab10-*, and *KIFC3*-deficient cells (Figs 6G and H, and 8A

and B). Since our findings did not completely rule out the possibility that cholesterol could access the ciliary membrane from the plasma membrane and the cytoplasmic membrane, it is safe to conclude that the peroxisomal Rabin8–Rab10–KIFC3 axis is a molecular mechanism of trafficking cholesterol to the ciliary membrane. Besides our screening candidates, several types of molecular machinery for peroxisome dynamics have been reported. For example, it was recently demonstrated that human mitochondrial Rho GTPase-1 (Miro1) localizes to peroxisomes to cooperate with the adaptor proteins TRAK1 and TRAK2, thereby mediating kinesin- and dynein-driven transport of peroxisomes in both directions (Castro *et al*, 2018b; Okumoto *et al*, 2018). Moreover, findings have suggested the occurrence of dynein-based minus-end-directed transport of peroxisomes in mammalian cells (Schrader *et al*, 2000). Further screens are thus needed to clarify the entire mechanism underlying the peroxisome dynamics to primary cilia for cholesterol trafficking. Taken together, our findings suggest that the diversity of intracellular cholesterol trafficking routes might contribute to the clinical heterogeneity of ciliopathy-related symptoms in NPC and ZS characterized by severe intracellular cholesterol accumulation.

How is cholesterol transferred from peroxisomal membranes to ciliary membranes? Although a more mechanistic understanding remains elusive, we suggest that the ciliary pocket membrane proteins EHD1 and EHD3 are involved in this step. It was previously shown that EHD1 and EHD3 cooperate with a SNARE membrane fusion regulator, SNAP29, to promote the Rab11–Rab8 cascade-mediated ciliary membrane assembly in the early stage of cilium formation (Lu *et al*, 2015). In the context of peroxisome-mediated cholesterol trafficking to the ciliary membrane, EHD1 and EHD3 physically interact with a peroxisomal membrane protein, PEX14 (Fig 3F–H), implying that they mediate the heterophilic organelle–organelle interaction between peroxisomes and primary cilia. Our time-lapse imaging data demonstrate that peroxisomes contact the region of the ciliary pocket for around 10–20 min, and that they are freely released from primary cilia after this contact. Based on our results, we speculate that the cholesterol transfer from peroxisomes to primary cilia might be mediated by not membrane fusions but membrane contacts. Here, we observed that pAkt (Ser 473) and EHD1/3 localize to discrete domains in the pocket membrane (Fig 3F), implying that the ciliary pocket might have different biochemical and physiological compartments. After peroxisomes are transported to the base of the cilium via microtubules, there are two potential mechanisms of the peroxisome and ciliary pocket interaction for cholesterol trafficking. The first is that the peroxisomes directly communicate with the EHD-rich ciliary pocket membrane. The second is that the peroxisomes interact with the bottom of the pAkt (Ser473)-labeled pocket membrane and then become associated with the EHD region of the ciliary pocket membrane. To verify these possibilities, there is a need to develop real-time microscopy technology with higher spatiotemporal resolution.

It was previously shown that, in mammalian cells, the integral lysosomal membrane protein synaptotagmin VII (Syt7) binds to the lipid PI(4,5)P2 on the peroxisomal membrane to form a membrane contact site, thereby transporting cholesterol from lysosomes to peroxisomes (Chu *et al*, 2015). Recently, it was also reported that a tethering complex of VAP-A/B on the endoplasmic reticulum (ER) and ACBD5 (acyl Co-A binding protein 5) or PEX16 on the peroxisomes forms a peroxisome–ER contact site in human cells for

peroxisome biogenesis, the biosynthesis of plasmalogens, and cholesterol homeostasis (Costello *et al*, 2017; Hua *et al*, 2017). In this study, we identified the ORP3 protein as a lipid transfer protein for the ciliary cholesterol trafficking from peroxisomes to primary cilia (Fig 5). Many ORP3-positive punctate signals were detected not only at the ciliary pocket, but also at other cellular regions (Fig 5E and H). Previous reports demonstrated that ORP3 localizes to the PM, ER, and endosomes (Lehto *et al*, 2005; Santos *et al*, 2018), suggesting that these structures have potency to transfer cholesterol to primary cilia. In contrast, the FRB-FKBP system-mediated peroxisome targeting to the ciliary pocket did not restore the ciliary cholesterol insufficiency in $ORP3^{-/-}$ hTERT-RPE1 cells (Fig 8A and B), suggesting that ORP3 is required for at least the peroxisome-mediated cholesterol trafficking into the ciliary membrane.

Our data demonstrate that peroxisomes do not enter the axonemal compartment in primary cilia (Appendix Fig S4 and Appendix Fig S5C), implying that, after the peroxisome–ciliary pocket contact, cholesterol might be transported in the ciliary membrane surrounding the axonemal region by another trafficking system. It was recently reported that a kinesin-3 family member, KIF13B, establishes a lipid raft microdomain enriched in the protein caveolin 1 at the ciliary transition zone (TZ), which is located between the basal body and cilium, to promote Shh signaling (Schou *et al*, 2017). Since cholesterol is an important component of lipid rafts formed in the PM (Lingwood & Simons, 2010), ciliary cholesterol might also contribute to the formation and physiological functions of the caveolin 1-enriched microdomain at the TZ. The LDL-mediated cholesterol compensation partially restored the ciliary phenotype in the ZS patient cells and ZS-modeled cells compared with the case in cholesterol-depleted conditions (Figs 1G and 2I), implying that unknown pathways for ciliary cholesterol trafficking might exist. Chu *et al* reported an excellent screening system to identify proteins critical for intracellular cholesterol trafficking using an antifungal antibiotic, amphotericin B, in which cells only survive when they have damaged intracellular cholesterol trafficking (Chu *et al*, 2015). In future, combined approaches of amphotericin B cell-based screening and genome-scale CRISPR/Cas9 knockout (GeCKO) libraries (Shalem *et al*, 2014) should enable us to uncover the molecular machinery behind intra-ciliary membrane cholesterol transport.

In conclusion, we demonstrate that the dynamics of peroxisomes along the microtubules via the PEX14–Rabin8–Rab10–KIFC3 complex are essential for the supply of cholesterol into ciliary membranes.

Materials and Methods

Cell cultures

Human primary skin fibroblasts from a normal individual (GM 22277; Coriell Institute), SLO patient (GM05788; Coriell Institute), ZS patients (GM16513 and GM17398; Coriell Institute), X-ALD patient (GM17819; Coriell Institute), and NPC patient (GM23151; Coriell Institute) were cultured in Dulbecco's modified Eagle's medium (DMEM; Gibco, Life Technologies) supplemented with 20% fetal bovine serum (FBS) and 50 mg/ml gentamycin. Genetic information on the skin fibroblasts from each patient and the

normal individual is described in STAR METHODS, key resource table. hTERT-RPE1 cells (ATCC CRL-4000), NIH3T3 cells, and HEK293T cells were maintained in DMEM with 10% FBS and 50 mg/ml gentamycin. All cells were grown at 37°C in humidified air with 5% CO_2.

Antibodies

The primary antibodies used were as follows: mouse anti-acetylated-tubulin monoclonal antibody mAb (T7451; Sigma-Aldrich); mouse anti-Smo mAb (sc-166685; Santa Cruz); rabbit anti-Arl13b polyclonal antibody pAb (17711-1-AP; Proteintech); rabbit anti-PEX1 pAb (13669-1-AP; Proteintech); rabbit anti-PEX14 pAb (10594-1-AP; Proteintech); rabbit anti-pericentrin pAb (A301-348A; Bethyl Laboratories); mouse anti-PMP70 mAb (SAB4200181; Sigma-Aldrich); mouse anti-ninein mAb (MABT29; Merck Millipore); mouse anti-GAPDH mAb (sc-32233; Santa Cruz Biotechnology); rabbit anti-GFP pAb (598; MBL); mouse anti-phospho-S473 Akt mAb (#4051; Cell Signaling Technology); mouse anti-GFP mAb (11-814-460-001; Roche); rabbit anti-Rabin8 pAb (12321-1-AP; Proteintech); rabbit anti-Rab10 pAb (27094-1-AP; Proteintech); rabbit anti-KIFC3 pAb (10125-2-AP; Proteintech); rat anti-α-tubulin mAb (NB600-506; Novus); mouse anti-γ-tubulin mAb (T6557; Sigma-Aldrich); mouse anti-CYPOR mAb (sc-25270; Santa Cruz); rabbit anti-NPC1 pAb (13926-1-AP; Proteintech); rabbit anti-ABCD1 pAb (18138-1-AP; Proteintech); rabbit anti-EHD1 pAb (24657-1-AP; Proteintech); rabbit anti-EHD3 pAb (25320-1-AP; Proteintech); rabbit anti-Shh pAb (ab53281; Abcam); mouse anti-ORP3 mAb (sc-398326; Santa Cruz); rabbit anti-ACOX1 pAb (10957-1-AP; Proteintech); goat anti-Patched 1 pAb (sc-6149; Santa Cruz); rabbit anti-ODF2 pAb (HPA001874; Sigma-Aldrich); and mouse anti-DYKDDDDK (FLAG) tag mAb (018-22381; Fujifilm Wako).

Plasmids

AcGFP1-tagged human *Pex14*, *Rabin8*, *Rab8B*, *Rab10*, and *KIFC3*, *AcGFP1*-tagged *D4-domain of perfringolysin O* (θ-*toxin*) from *Clostridium perfringens*, *DsRed2*-tagged *PACT* (the C-terminal region of human pericentrin 3097–3336 a.a.) and *Smo*, and *3×FLAG*-tagged human *Pex14*, *Rab10*, *EHD1*, *EHD3*, *ORP3*, and *KIFC3* expression vectors for mammalian cells were constructed by PCR and standard cloning techniques. We also used site-directed mutagenesis to insert mutations into *Rab8B* and *Rab10*. *ECFP-SKL* (#54548), *GFP-Rab8A* (#24898), *GFP-Rab8A-Q67L* (#24900), and *tdTomato-BicD2-FKBP* (#64205) expression vectors were purchased from Addgene. The *PEX3-GFP-FRB* expression vector for mammalian cells was constructed from *PEX3-GFP-Halo* (#67764; Addgene) and *Mito-mCherry-FRB* (#59352; Addgene) using PCR and the Gibson assembly kit (New England Biolabs). *GFP-MCHR1* was previously constructed as reported elsewhere (Hamamoto *et al*, 2016). All mutations were verified by automated sequencing. For the construction of an expression vector of both sgRNA targeting gene and *spCas9*, a pair of annealed oligodeoxynucleotides designed on the target sites addressed in the key resource table with overhangs of the BbsI restriction enzyme site were inserted into the *pX330-U6-Chimeric_BB-CBh-hSpCas9* plasmid (#42230; Addgene). The targeting plasmid vector contained a BbsI restriction enzyme site flanked with a CMV promoter-driven *hsvTK-2A-*

Neo cassette, as described previously (Miyamoto *et al*, 2015), in the multi-cloning site of *pBluescript SK II*$^+$. A pair of oligodeoxynucleotides recognized by the CRISPR/Cas9 system for the target site (Appendix Table S1) were ligated into the targeting vector backbone mediated by the BbsI restriction enzyme site. Successful integration of oligodeoxynucleotides into each plasmid vector was verified by Sanger sequencing.

Gene targeting in hTERT-RPE1 cells using the CRISPR/ObLiGaRe method

A total of 2×10^5 hTERT-RPE1 cells were seeded into one well of a six-well plate 24 h before lipofection. Then, 20 ng of the targeting vector and 600 ng of the *pX330* plasmid vector for the target gene editing were transfected into the cells using Lipofectamine LTX (ThermoFisher), in accordance with the manufacturer's protocol. At 48 h after the transfection, the transfected cells were reseeded into 15-cm dishes and then subjected to selection using 2 mg/ml G418 (Nacalai Tesque). Eight to sixteen drug-resistant cell colonies were then picked up on days 14–18 after transfection. These colonies were divided into two aliquots: One was transferred into a well of a 96-well plate for clonal expansion, while the other was lysed and used for PCR and direct-sequence genotyping. As described previously (Royba *et al*, 2017), PCR genotyping to screen the hTERT-RPE1 cell clones was performed using extracted genomic DNA as a template and KOD-FX Neo DNA polymerase (Toyobo) with three types of primer pair: the first primer pair for detecting the target gene locus (Appendix Table S1), the second primer pair consisting of the forward primer in the target gene locus and *Neo*^{r}-reverse primer (5′-GCGGATCTGACGGTTCAC-TAAACCAGC-3′) for detecting the forward insertion of the drug-resistant gene cassette into the target gene locus, and the third primer pair consisting of the reverse primer in the target gene locus and *Neo*^{r}-reverse primer for detecting the reversed insertion. PCR products were run on 2.0% agarose gel. The wild-type-sized PCR products amplified with the third primer pair were directly sequenced to determine the presence or absence of insertion or deletion mutations using 3130 Genetic Analyzer (Applied Biosystems). The efficiency of gene targeting using this method is dependent on the gene locus. In this study, the average efficacies of gene knockout in the G418-resistant clones were 40–75%.

Immunoprecipitation and Western blot analyses

Cells were transfected with plasmid DNA for immunoprecipitation analysis and cultured in serum-free DMEM for 24 h. The cells were lysed in lysis buffer (0.5% Triton X-100, 150 mM NaCl, 20 mM Tris–HCl pH 7.5, 1 mM EDTA, 0.5 mM PMSF, 2 mg/ml pepstatin A, 10 mg/ml leupeptin, 5 mg/ml aprotinin). The lysates were sheared with a 21-gauge needle, incubated on ice for 15 min, and clarified by centrifugation at 20,817 *g* for 15 min at 4°C. The supernatants were precleared with protein A/G-conjugated agarose beads (Santa Cruz) and incubated with anti-FLAG antibody covalently conjugated agarose beads (012-22781; Fujifilm Wako); the mixtures were then rotated for a further 16 h at 4°C. The agarose beads were washed three times with wash buffer (1% Nonidet P-40, 0.1% SDS, 0.5% deoxycholate, 150 mM NaCl, 50 mM Tris–HCl pH 7.5, 1 mM EDTA, 0.5 mM PMSF, 2 mg/ml pepstatin A, 10 mg/ml leupeptin, 5 mg/ml

aprotinin) before elution with sample buffer. The immunoprecipitates were analyzed by 10% SDS–PAGE and transferred to PVDF membranes for Western blot analyses, as described previously (Miyamoto *et al*, 2015). Here, 15% IP fractions and 0.75% inputs were detected by Western blotting. For the validation of gene knock-out, 1.5% cell lysate was applied to each lane.

In vitro binding analysis

GST (0.2 μg, Abcam: ab81793) or GST fused to PEX14 proteins (1 μg, Abnova: H00005195-P01) was loaded to glutathione-Sepharose beads (GE Healthcare) and then incubated with 6×His-EHD3 (1 μg, ORIGENE: TP761227), 6×His-Rabin8 (1 μg, ORIGENE: TP760069), or 6×His-Rab10 (1 μg, NOVUS: NBP2-23392). The mixtures were then rotated for 2 h at 4°C in an *in vitro* binding buffer (50 mM Tris–HCl pH7.5, 150 mM NaCl, 1% Triton X-100, 1 mM dithiothreitol, 1 mM EDTA, 10% glycerol, 0.5 mM PMSF, 2 mg/ml pepstatin A, 10 mg/ml leupeptin, 5 mg/ml aprotinin). The glutathione-Sepharose beads were washed three times with the *in vitro* binding buffer minus glycerol before elution with sample buffer. Bound and input proteins were analyzed by SDS–PAGE and Western blotting. Here, 15% pull-down fractions and 0.75% inputs were detected by Western blotting.

Immunofluorescence microscopy

For detection of the protein epitopes, cells grown on coverslips (Matsunami Glass) were fixed in 4% paraformaldehyde at room temperature for 15 min or 100% methanol at −20°C for 10 min, permeabilized in 0.2% Triton X-100, briefly washed with PBS three times, blocked with 1% BSA in PBS for 30 min, and probed with primary antibodies. Antibody–antigen complexes were detected with Alexa Fluor 405-, Alexa Fluor 594-, Alexa Fluor 488-, or Alexa Fluor 647-conjugated goat or guinea pig secondary antibodies (ThermoFisher) by incubation for 30 min at room temperature. The cells were washed three times with PBS and then counterstained with 4′,6′-diamidino-2-phenylindole (DAPI). For the detection of intracellular cholesterol, the serum-starved cells transfected with or without the *AcGFP1-D4* expression vector were fixed in 4% paraformaldehyde at room temperature for 15 min, briefly washed with PBS three times, blocked with 1% BSA in PBS for 30 min, and incubated with 50 μg/ml Filipin III (Cayman Chemical) in Can Get Signal immunostain solution A (Toyobo) and each antibody for counterstaining at room temperature for 1 h. Antibody–antigen complexes were detected with Alexa Fluor 594-, Alexa Fluor 488-, or Alexa Fluor 647-conjugated goat secondary antibodies (ThermoFisher) by incubation for 3 min at room temperature. The cells were washed three times with PBS and then mounted with Prolong Diamond anti-fader medium (ThermoFisher) or Vectashield mounting medium (Vector laboratories). Immuno- and/or Filipin III-stained cells were examined under a fluorescence microscope (BZ9000; Keyence), a confocal microscope (LSM800; Carl Zeiss Microimaging Inc.), or 3D-structured illumination microscopes (Elyra PS1 microscope; Carl Zeiss Microimaging Inc., Deltavision OMX SR; GE Healthcare). Obtained confocal images were 3D-reconstituted using Imaris software (Bitplane). For evaluation of the ciliary cholesterol and proteins, ImageJ software was used for measurement of ciliary signal intensity in the images captured with a confocal microscope

(LSM800; Carl Zeiss Microimaging Inc.). Acetylated-tubulin signal-positive areas were regarded as cilia; the mean of ciliary Filipin III, Smo, and AcGFP1-D4 pixel intensity was determined by the value of total ciliary pixel intensity per area of cilia. Each measurement was performed in a single plane with a clear acetylated-tubulin signal. The value of background intensity outside cells was subtracted from each ciliary intensity.

Time-lapse imaging

The sets of expression vectors (*EGFP-MCHR1*, *ECFP-SKL*, and *DsRed2-PACT*; *AcGFP1-EHD1*, *ECFP-SKL*, and *DsRed2-Smo*) were transfected to hTERT-RPE1 cells grown on glass-bottomed dishes (Matsunami Glass) using Lipofectamine LTX reagent (Thermo-Fisher). At 24 h after transfection, the medium was replaced with serum-free DMEM and then cells were incubated for 24 h to induce ciliogenesis. Cells were monitored with a confocal microscope (LSM800; Carl Zeiss Microimaging Inc.) in a moisture chamber (Tokai Hit) at 37°C in humidified air with 5% CO_2. Images through each color filter were simultaneously acquired. Z-stack images were captured at 5-min intervals for 2 h, and overlapping images and movies were created using ZEN software (Carl Zeiss Microimaging Inc.).

Cholesterol depletion and rescue experiments

To remove intracellular cholesterol, confluent cells were incubated in serum-free DMEM for 24 h, after which they were treated for 45 min with 1.5% methyl-β-cyclodextrin (Sigma-Aldrich) in DMEM. All subsequent incubations were performed in DMEM containing 40 μM pravastatin to attenuate cholesterol biosynthesis, with or without the indicated additives. For cholesterol complementation assays, cholesterol was delivered by incubating the cells for 1 h with 50 μM or 100 μM water-soluble methyl-β-cyclodextrin–cholesterol complex (Sigma-Aldrich) in DMEM supplemented with 40 μM pravastatin. Alternatively, cholesterol was compensated for by incubating the cells with 0.06 mg/ml LDL (Sigma-Aldrich) in DMEM supplemented with 40 μM pravastatin and the desired agents. The cells were then treated for 24 h with the desired agents and subsequently processed for immunofluorescence analyses.

Shh pathway assay

For qPCR assays, confluent skin fibroblasts in 96-well plates were cultured in serum-free DMEM for 24 h, after which they were incubated for 24 h in serum-free DMEM containing 1 μM SAG (EMD Millipore™ Calbiochem™). The cells were washed with ice-cold PBS, lysed, and then, cDNAs were synthesized with reverse transcriptase from their extracted total RNA using Cells-to-CT Kit (ThermoFisher), in accordance with the manufacturer's protocol. Expression was measured by TaqMan PCR analysis using *Gli1* and *β-actin* TaqMan probes (ThermoFisher) on a CFX Connect™ Real-Time PCR Detection System (Bio-Rad); the levels of *Gli1* expression were normalized to those of *β-actin*. The primers and Taqman probes were *Gli1* (Hs00171790_m1) and *β-Actin* (Hs01060665_g1). All qPCR assays were performed in triplicate starting from three cell cultures, with error bars indicating SD. For evaluation of the ciliary localization of Smo, confluent cells grown on coverslips were

cultured in serum-free DMEM for 24 h, after which they were incubated for 24 h in serum-free DMEM with 50 nM Shh-N (EMD Millipore™ Calbiochem™). Shh-N-stimulated cells were immuno fluorescently stained as described above. The primary antibodies used were as follows: mouse monoclonal anti-acetylated-tubulin IgG2b isotype (T7451, 1:500 dilution; Sigma-Aldrich), mouse monoclonal anti-Smo IgG2a isotype (sc-166685, 1:200 dilution; Santa Cruz), and mouse monoclonal anti-γ-tubulin monoclonal IgG1 isotype (T6557, 1:500 dilution; Sigma-Aldrich).

MCH-dependent ciliary shortening assay

MCHR1-EGFP expression vector (Hamamoto *et al*, 2016) was transfected to hTERT-RPE1 cells grown on coverslips (Matsunami Glass) using Lipofectamine LTX reagent (ThermoFisher). At 24 h after transfection, the medium was replaced with serum-free DMEM, and then, cells were incubated for 24 h to induce ciliogenesis. The ciliated cells were incubated in DMEM containing 1 μM MCH (Peptide Institute) for 6 h and then processed for the immunofluorescence analysis.

Fractionation of peroxisomes

Peroxisome fractions were isolated using a Peroxisome isolation kit (Sigma-Aldrich), in accordance with the manufacturer's protocol. Cells were collected by centrifugation at 250 g for 5 min at 4°C and cell pellets were homogenized using a pestle in 1×Peroxisome Extraction Buffer (5 mM MOPS, pH 7.65, 1.25 M sucrose, 5 mM EDTA, 0.5% ethanol). After centrifugation at 25,000 *g* for 20 min at 4°C, the supernatants were removed and the pellets were suspended in 1×Peroxisome Extraction Buffer to obtain the Crude Peroxisome Fraction (CPF). OptiPrep Density Gradient Medium (60% solution of iodixanol in water) was diluted to 22.5% and 27.5% iodixanol concentration using 1×Optiprep Dilution Buffer (5 mM MOPS, pH 8.0, 1 mM EDTA, 0.1% ethanol). Diluted OptiPrep Density Gradient Medium was applied to an ultracentrifuge tube, onto which CPF was overlaid. Tubes were centrifuged at 100,000 *g* for 1.5 h at 4°C, and the bottom layer was collected as the peroxisome fraction. Finally, 0.05% and 0.5% total cell lysates, 0.75% crude peroxisome fraction (CPF), 0.4% lysosome/mitochondria fraction (Lyso/Mit) fraction, and 0.5% peroxisome fraction (PEX) obtained by this procedure were applied and detected by Western blotting.

Rapamycin-induced targeting of peroxisomes to the ciliary pocket

PEX3-GFP-FRB and *tdTomato-BicD2-FKBP* expression vectors were co-transfected to hTERT-RPE1 cells grown on coverslips (Matsunami Glass) using Lipofectamine LTX reagent (ThermoFisher). At 24 h after transfection, the medium was replaced with serum-free DMEM, and then, cells were incubated for 24 h to induce ciliogenesis. The ciliated cells were incubated in DMEM containing 100 μM rapamycin (LC Laboratories) for 30 min and then processed for the Filipin III staining and immunofluorescence analyses.

Quantification of intracellular cholesterol levels

Total cellular cholesterol and free cholesterol were measured using a Total Cholesterol and Cholesteryl Ester Colorimetric/Fluorometric

Assay Kit (BioVision), in accordance with the manufacturer's protocol. Human primary skin fibroblasts cultured in DMEM containing 20% FBS were collected by centrifugation at 250 *g* and room temperature and lysed in chloroform:isopropanol:NP-40 (7:11:0.1). After homogenization, extracts were centrifuged at 15,000 *g* and room temperature and cell debris was removed. Collected organic phases were dried at 50°C to remove chloroform and placed in a vacuum for 30 min. Dried lipid was dissolved with cholesterol assay buffer. Cholesterol probe, cholesterol enzyme mix, and cholesterol esterase were added to lipid samples and transferred to a 96-well plate, followed by incubation at 37°C for 1 h. For the detection of free cholesterol, cholesterol esterase-free samples were prepared. Fluorescence was determined using Varioskan (ThermoFisher). Values were normalized to the total amount of cell protein.

Three-dimensional FIB-SEM analysis

For the CLEM analysis, cells were seeded on gridded glass-bottomed dishes (MatTek). Before imaging by light microscopy, cell were fixed with 4% paraformaldehyde in sodium cacodylate buffer. Images were obtained with a FV3000 confocal laser scanning microscope (Olympus) with a U Plan Super Apochromat 60× oil objective. After imaging with light microscopy, cells were fixed with 2% glutaraldehyde in sodium cacodylate buffer and then stained with conventional en bloc procedure (Willingham & Rutherford, 1984) with uranyl acetate and lead aspartate. Cells were dehydrated in graded series of ethanol and embedded in Epon812 (4:6) epoxy resin (TAAB). The region of interest was trimmed and mounted onto the metal pin for FIB-SEM. Before loading into the vacuum chamber of FIB-SEM, samples were coated with carbon using a Q150T sputter coater (Quorum Technologies).

FIB-SEM tomography was carried out using a Helios G4 UC Dual Beam system and Auto Slice and View software (Thermo Fisher Scientific). Serial milling at 10-nm intervals was obtained at 30 kV and 83 pA, and subsequent SEM imaging of the block face was performed at 1.5 kV and 100 pA using the in-column BSE detector. Obtained serial images with the voxel size of 4 × 4 × 10 nm were reconstructed and manually segmented using the Amira software Ver.5.6 (Thermo Fisher Scientific).

Statistical analysis

All experiments were performed independently at least three times. The data are shown as mean ± s.d., at least carried out in triplicate. Differences between groups were evaluated for statistical significance using one-way analysis of variance (ANOVA) followed by Tukey's post hoc tests (Tukey's HSD). The software of R version 3.4.4 was used. Values of $P < 0.05$ were considered to be statistically significant.

Data availability

Raw data and CRISPR/Cas9-mediated knockout cells associated with the figures will be made available on a reasonable request.

Expanded View for this article is available online.

Acknowledgments

Author contributions

TM, KH, TI, AHI, SNA, and HO performed experiments and analyzed data. TM conceived the study. AHI, YS, TY, and SM supervised the study. TM, KH, TI, AHI, and SM wrote the paper. All authors interpreted data.

Conflict of interest

The authors declare that they have no conflict of interest.

References

Abe S, Nagai T, Masukawa M, Okumoto K, Homma Y, Fujiki Y, Mizuno K (2017) Localization of protein kinase NDR2 to peroxisomes and its role in ciliogenesis. *J Biol Chem* 292: 4089–4098

Argyriou C, D'Agostino MD, Braverman N (2016) Peroxisome biogenesis disorders. *Transl Sci Rare Dis* 1: 111–144

Baker K, Beales PL (2009) Making sense of cilia in disease: the human ciliopathies. *Am J Med Genet C Semin Med Genet* 151C: 281–295

Benmerah A (2013) The ciliary pocket. *Curr Opin Cell Biol* 25: 78–84

Blassberg R, Macrae JI, Briscoe J, Jacob J (2016) Reduced cholesterol levels impair Smoothened activation in Smith-Lemli-Opitz syndrome. *Hum Mol Genet* 25: 693–705

Breslow DK, Koslover EF, Seydel F, Spakowitz AJ, Nachury MV (2013) An *in vitro* assay for entry into cilia reveals unique properties of the soluble diffusion barrier. *J Cell Biol* 203: 129–147

Brown MS, Goldstein JL (1986) A receptor-mediated pathway for cholesterol homeostasis. *Science* 232: 34–47

Byrne EFX, Sircar R, Miller PS, Hedger G, Luchetti G, Nachtergaele S, Tully MD, Mydock-McGrane L, Covey DF, Rambo RP *et al* (2016) Structural basis of Smoothened regulation by its extracellular domains. *Nature* 535: 517–522

Carstea ED, Morris JA, Coleman KG, Loftus SK, Zhang D, Cummings C, Gu J, Rosenfeld MA, Pavan WJ, Krizman DB *et al* (1997) Niemann-Pick C1 disease gene: homology to mediators of cholesterol homeostasis. *Science* 277: 228–231

Castro IG, Richards DM, Metz J, Costello JL, Passmore JB, Schrader TA, Gouveia A, Ribeiro D, Schrader M (2018b) A role for Mitochondrial Rho GTPase 1 (MIRO1) in motility and membrane dynamics of peroxisomes. *Traffic* 19: 229–242

Castro IG, Schuldiner M, Zalckvar E (2018a) Mind the organelle gap – peroxisome contact sites in disease. *Trends Biochem Sci* 43: 199–210

Chailley B, Boisvieux-Ulrich E, Sandoz D (1983) Evolution of filipin-sterol complexes and intramembrane particle distribution during ciliogenesis. *J Submicrosc Cytol* 15: 275–280

Chailley B, Boisvieux-Ulrich E (1985) Detection of plasma membrane cholesterol by filipin during microvillogenesis and ciliogenesis in quail oviduct. *J Histochem Cytochem* 33: 1–10

Chang TY, Chang CC, Cheng D (1997) Acyl-coenzyme A:cholesterol acyltransferase. *Annu Rev Biochem* 66: 613–638

Chang CC, South S, Warren D, Jones J, Moser AB, Moser HW, Gould SJ (1999) Metabolic control of peroxisome abundance. *J Cell Sci* 112(Pt 10): 1579–1590

Chu BB, Liao YC, Qi W, Xie C, Du X, Wang J, Yang H, Miao HH, Li BL, Song BL (2015) Cholesterol transport through lysosome-peroxisome membrane contacts. *Cell* 161: 291–306

Corbit KC, Aanstad P, Singla V, Norman AR, Stainier DY, Reiter JF (2005) Vertebrate Smoothened functions at the primary cilium. *Nature* 437: 1018–1021

Costello JL, Castro IG, Hacker C, Schrader TA, Metz J, Zeuschner D, Azadi AS, Godinho LF, Costina V, Findeisen P *et al* (2017) ACBD5 and VAPB mediate membrane associations between peroxisomes and the ER. *J Cell Biol* 216: 331–342

Das A, Goldstein JL, Anderson DD, Brown MS, Radhakrishnan A (2013) Use of mutant 125I-perfringolysin O to probe transport and organization of cholesterol in membranes of animal cells. *Proc Natl Acad Sci USA* 110: 10580–10585

Dietrich D, Seiler F, Essmann F, Dodt G (2013) Identification of the kinesin KifC3 as a new player for positioning of peroxisomes and other organelles in mammalian cells. *Biochim Biophys Acta* 1833: 3013–3024

Fitzky BU, Witsch-Baumgartner M, Erdel M, Lee JN, Paik YK, Glossmann H, Utermann G, Moebius FF (1998) Mutations in the Delta7-sterol reductase gene in patients with the Smith-Lemli-Opitz syndrome. *Proc Natl Acad Sci USA* 95: 8181–8186

FitzPatrick DR (1996) Zellweger syndrome and associated phenotypes. *J Med Genet* 33: 863–868

Folz SJ, Trobe JD (1991) The peroxisome and the eye. *Surv Ophthalmol* 35: 353–368

Formichi P, Battisti C, De Santi MM, Guazzo R, Tripodi SA, Radi E, Rossi B, Tarquini E, Federico A (2018) Primary cilium alterations and expression changes of Patched1 proteins in niemann-pick type C disease. *J Cell Physiol* 233: 663–672

Fujiki Y (2016) Peroxisome biogenesis and human peroxisome-deficiency disorders. *Proc Jpn Acad Ser B Phys Biol Sci* 92: 463–477

Garcia G III, Raleigh DR, Reiter JF (2018) How the ciliary membrane is organized inside-out to communicate outside-in. *Curr Biol* 28: R421–R434

Garcia-Gonzalo FR, Phua SC, Roberson EC, Garcia G 3rd, Abedin M, Schurmans S, Inoue T, Reiter JF (2015) Phosphoinositides regulate ciliary protein trafficking to modulate hedgehog signaling. *Dev Cell* 34: 400–409

Goetz SC, Anderson KV (2010) The primary cilium: a signalling centre during vertebrate development. *Nat Rev Genet* 11: 331–344

Gronemeyer T, Wiese S, Grinhagens S, Schollenberger L, Satyagraha A, Huber LA, Meyer HE, Warscheid B, Just WW (2013) Localization of Rab proteins to peroxisomes: a proteomics and immunofluorescence study. *FEBS Lett* 587: 328–338

Hamamoto A, Yamato S, Katoh Y, Nakayama K, Yoshimura K, Takeda S, Kobayashi Y, Saito Y (2016) Modulation of primary cilia length by melanin-concentrating hormone receptor 1. *Cell Signal* 28: 572–584

Homma Y, Fukuda M (2016) Rabin8 regulates neurite outgrowth in both GEF activity-dependent and -independent manners. *Mol Biol Cell* 27: 2107–2118

Hua R, Cheng D, Coyaud E, Freeman S, Di Pietro E, Wang Y, Vissa A, Yip CM, Fairn GD, Braverman N *et al* (2017) VAPs and ACBD5 tether peroxisomes to the ER for peroxisome maintenance and lipid homeostasis. *J Cell Biol* 216: 367–377

Huang P, Nedelcu D, Watanabe M, Jao C, Kim Y, Liu J, Salic A (2016) Cellular cholesterol directly activates smoothened in hedgehog signaling. *Cell* 166 (1176–1187): e14

Huang P, Zheng S, Wierbowski BM, Kim Y, Nedelcu D, Aravena L, Liu J, Kruse AC, Salic A (2018) Structural basis of smoothened activation in hedgehog signaling. *Cell* 174: 312–324.e16

Hui CC, Angers S (2011) Gli proteins in development and disease. *Annu Rev Cell Dev Biol* 27: 513–537

Ikonen E (2008) Cellular cholesterol trafficking and compartmentalization. *Nat Rev Mol Cell Biol* 9: 125–138

Ishibashi S, Schwarz M, Frykman PK, Herz J, Russell DW (1996) Disruption of cholesterol 7alpha-hydroxylase gene in mice. I. Postnatal lethality reversed by bile acid and vitamin supplementation. *J Biol Chem* 271: 18017–18023

Ishikawa H, Marshall WF (2011) Ciliogenesis: building the cell's antenna. *Nat Rev Mol Cell Biol* 12: 222–234

Ishikawa H, Thompson J, Yates JR III, Marshall WF (2012) Proteomic analysis of mammalian primary cilia. *Curr Biol* 22: 414–419

Kanerva K, Uronen RL, Blom T, Li S, Bittman R, Lappalainen P, Peranen J, Raposo G, Ikonen E (2013) LDL cholesterol recycles to the plasma membrane via a Rab8a-Myosin5b-actin-dependent membrane transport route. *Dev Cell* 27: 249–262

Kinnebrew M, Iverson EJ, Patel BB, Pusapati GV, Kong JH, Johnson KA, Luchetti G, Eckert KM, McDonald JG, Covey DF *et al* (2019) Cholesterol accessibility at the ciliary membrane controls hedgehog signaling. *Elife* 8, e50051

Klouwer FC, Berendse K, Ferdinandusse S, Wanders RJ, Engelen M, Poll-The BT (2015) Zellweger spectrum disorders: clinical overview and management approach. *Orphanet J Rare Dis* 10: 151

Kohli P, Hohne M, Jungst C, Bertsch S, Ebert LK, Schauss AC, Benzing T, Rinschen MM, Schermer B (2017) The ciliary membrane-associated proteome reveals actin-binding proteins as key components of cilia. *EMBO Rep* 18: 1521–1535

Kwon HJ, Abi-Mosleh L, Wang ML, Deisenhofer J, Goldstein JL, Brown MS, Infante RE (2009) Structure of N-terminal domain of NPC1 reveals distinct subdomains for binding and transfer of cholesterol. *Cell* 137: 1213–1224

Lange Y, Ye J, Rigney M, Steck TL (1999) Regulation of endoplasmic reticulum cholesterol by plasma membrane cholesterol. *J Lipid Res* 40: 2264–2270

Lehto M, Hynynen R, Karjalainen K, Kuismanen E, Hyvarinen K, Olkkonen VM (2005) Targeting of OSBP-related protein 3 (ORP3) to endoplasmic reticulum and plasma membrane is controlled by multiple determinants. *Exp Cell Res* 310: 445–462

Lingwood D, Simons K (2010) Lipid rafts as a membrane-organizing principle. *Science* 327: 46–50

Liscum L, Faust JR (1989) The intracellular transport of low density lipoprotein-derived cholesterol is inhibited in Chinese hamster ovary cells cultured with 3-beta-[2-(diethylamino)ethoxy]androst-5-en-17-one. *J Biol Chem* 264: 11796–11806

Lopez CA, de Vries AH, Marrink SJ (2011) Molecular mechanism of cyclodextrin mediated cholesterol extraction. *PLoS Comput Biol* 7: e1002020

Lu Q, Insinna C, Ott C, Stauffer J, Pintado PA, Rahajeng J, Baxa U, Walia V, Cuenca A, Hwang YS *et al* (2015) Early steps in primary cilium assembly require EHD1/EHD3-dependent ciliary vesicle formation. *Nat Cell Biol* 17: 228–240

Luchetti G, Sircar R, Kong JH, Nachtergaele S, Sagner A, Byrne EF, Covey DF, Siebold C, Rohatgi R (2016) Cholesterol activates the G-protein coupled receptor Smoothened to promote Hedgehog signaling. *Elife* 5: e20304

Luisiri A, Sotelo-Avila C, Silberstein MJ, Graviss ER (1988) Sonography of the Zellweger syndrome. *J Ultrasound Med* 7: 169–173

Maresca M, Lin VG, Guo N, Yang Y (2013) Obligate ligation-gated recombination (ObLiGaRe): custom-designed nuclease-mediated targeted integration through nonhomologous end joining. *Genome Res* 23: 539–546

Matsumoto Y, Morishima K, Honda A, Watabe S, Yamamoto M, Hara M, Hasui M, Saito C, Takayanagi T, Yamanaka T *et al* (2005) R352Q mutation of the DHCR7 gene is common among Japanese Smith-Lemli-Opitz syndrome patients. *J Hum Genet* 50: 353–356

Ming JE, Roessler E, Muenke M (1998) Human developmental disorders and the Sonic hedgehog pathway. *Mol Med Today* 4: 343–349

Miyamoto T, Hosoba K, Ochiai H, Royba E, Izumi H, Sakuma T, Yamamoto T, Dynlacht BD, Matsuura S (2015) The microtubule-depolymerizing activity of a mitotic kinesin protein KIF2A drives primary cilia disassembly coupled with cell proliferation. *Cell Rep* 10: 664–673

Molla-Herman A, Ghossoub R, Blisnick T, Meunier A, Serres C, Silbermann F, Emmerson C, Romeo K, Bourdoncle P, Schmitt A *et al* (2010) The ciliary pocket: an endocytic membrane domain at the base of primary and motile cilia. *J Cell Sci* 123: 1785–1795

Mosser J, Douar AM, Sarde CO, Kioschis P, Feil R, Moser H, Poustka AM, Mandel JL, Aubourg P (1993) Putative X-linked adrenoleukodystrophy gene shares unexpected homology with ABC transporters. *Nature* 361: 726–730

Muenke M, Beachy PA (2000) Genetics of ventral forebrain development and holoprosencephaly. *Curr Opin Genet Dev* 10: 262–269

Myers BR, Neahring L, Zhang Y, Roberts KJ, Beachy PA (2017) Rapid, direct activity assays for Smoothened reveal Hedgehog pathway regulation by membrane cholesterol and extracellular sodium. *Proc Natl Acad Sci USA* 114: E11141–E11150

Nachury MV, Loktev AV, Zhang Q, Westlake CJ, Peranen J, Merdes A, Slusarski DC, Scheller RH, Bazan JF, Sheffield VC *et al* (2007) A core complex of BBS proteins cooperates with the GTPase Rab8 to promote ciliary membrane biogenesis. *Cell* 129: 1201–1213

Nachury MV (2018) The molecular machines that traffic signaling receptors into and out of cilia. *Curr Opin Cell Biol* 51: 124–131

Naureckiene S, Sleat DE, Lackland H, Fensom A, Vanier MT, Wattiaux R, Jadot M, Lobel P (2000) Identification of HE1 as the second gene of Niemann-Pick C disease. *Science* 290: 2298–2301

Nigg EA, Raff JW (2009) Centrioles, centrosomes, and cilia in health and disease. *Cell* 139: 663–678

Nowaczyk MJ, Irons MB (2012) Smith-Lemli-Opitz syndrome: phenotype, natural history, and epidemiology. *Am J Med Genet C Semin Med Genet* 160C: 250–262

Ohno-Iwashita Y, Shimada Y, Waheed AA, Hayashi M, Inomata M, Nakamura M, Maruya M, Iwashita S (2004) Perfringolysin O, a cholesterol-binding cytolysin, as a probe for lipid rafts. *Anaerobe* 10: 125–134

Okumoto K, Ono T, Toyama R, Shimomura A, Nagata A, Fujiki Y (2018) New splicing variants of mitochondrial Rho GTPase-1 (Miro1) transport peroxisomes. *J Cell Biol* 217: 619–633

Portsteffen H, Beyer A, Becker E, Epplen C, Pawlak A, Kunau WH, Dodt G (1997) Human PEX1 is mutated in complementation group 1 of the peroxisome biogenesis disorders. *Nat Genet* 17: 449–452

Reiter JF, Leroux MR (2017) Genes and molecular pathways underpinning ciliopathies. *Nat Rev Mol Cell Biol* 18: 533–547

Reuber BE, Germain-Lee E, Collins CS, Morrell JC, Ameritunga R, Moser HW, Valle D, Gould SJ (1997) Mutations in PEX1 are the most common cause of peroxisome biogenesis disorders. *Nat Genet* 17: 445–448

Rohatgi R, Milenkovic L, Scott MP (2007) Patched1 regulates hedgehog signaling at the primary cilium. *Science* 317: 372–376

Rossi A, Kontarakis Z, Gerri C, Nolte H, Holper S, Kruger M, Stainier DY (2015) Genetic compensation induced by deleterious mutations but not gene knockdowns. *Nature* 524: 230–233

Royba E, Miyamoto T, Natsuko Akutsu S, Hosoba K, Tauchi H, Kudo Y, Tashiro S, Yamamoto T, Matsuura S (2017) Evaluation of ATM heterozygous mutations underlying individual differences in radiosensitivity using genome editing in human cultured cells. *Sci Rep* 7: 5996

Santos MF, Rappa G, Karbanova J, Kurth T, Corbeil D, Lorico A (2018) VAMP-associated protein-A and oxysterol-binding protein-related protein 3 promote the entry of late endosomes into the nucleoplasmic reticulum. *J Biol Chem* 293: 13834–13848

Schou KB, Mogensen JB, Morthorst SK, Nielsen BS, Aleliunaite A, Serra-Marques A, Furstenberg N, Saunier S, Bizet AA, Veland IR *et al* (2017) KIF13B establishes a CAV1-enriched microdomain at the ciliary transition zone to promote Sonic hedgehog signalling. *Nat Commun* 8: 14177

Schrader M, King SJ, Stroh TA, Schroer TA (2000) Real time imaging reveals a peroxisomal reticulum in living cells. *J Cell Sci* 113(Pt 20): 3663–3671

Shalem O, Sanjana NE, Hartenian E, Shi X, Scott DA, Mikkelson T, Heckl D, Ebert BL, Root DE, Doench JG *et al* (2014) Genome-scale CRISPR-Cas9 knockout screening in human cells. *Science* 343: 84–87

Simons K, Ikonen E (2000) How cells handle cholesterol. *Science* 290: 1721–1726

Sleat DE, Wiseman JA, El-Banna M, Price SM, Verot L, Shen MM, Tint GS, Vanier MT, Walkley SU, Lobel P (2004) Genetic evidence for nonredundant functional cooperativity between NPC1 and NPC2 in lipid transport. *Proc Natl Acad Sci USA* 101: 5886–5891

Suizu F, Hirata N, Kimura K, Edamura T, Tanaka T, Ishigaki S, Donia T, Noguchi H, Iwanaga T, Noguchi M (2016) Phosphorylation-dependent Akt-Inversin interaction at the basal body of primary cilia. *EMBO J* 35: 1346–1363

Teglund S, Toftgard R (2010) Hedgehog beyond medulloblastoma and basal cell carcinoma. *Biochim Biophys Acta* 1805: 181–208

Vance JE, Vance DE (1990) Lipoprotein assembly and secretion by hepatocytes. *Annu Rev Nutr* 10: 337–356

Varjosalo M, Li SP, Taipale J (2006) Divergence of hedgehog signal transduction mechanism between Drosophila and mammals. *Dev Cell* 10: 177–186

Wanders RJ (2014) Metabolic functions of peroxisomes in health and disease. *Biochimie* 98: 36–44

Wassif CA, Maslen C, Kachilele-Linjewile S, Lin D, Linck LM, Connor WE, Steiner RD, Porter FD (1998) Mutations in the human sterol delta7-reductase gene at 11q12-13 cause Smith-Lemli-Opitz syndrome. *Am J Hum Genet* 63: 55–62

Waterham HR, Ferdinandusse S, Wanders RJ (2016) Human disorders of peroxisome metabolism and biogenesis. *Biochim Biophys Acta* 1863: 922–933

Willingham MC, Rutherford AV (1984) The use of osmium-thiocarbohydrazide-osmium (OTO) and ferrocyanide-reduced osmium methods to enhance membrane contrast and preservation in cultured cells. *J Histochem Cytochem* 32: 455–460

Xiao X, Tang JJ, Peng C, Wang Y, Fu L, Qiu ZP, Xiong Y, Yang LF, Cui HW, He XL *et al* (2017) Cholesterol modification of smoothened is required for hedgehog signaling. *Mol Cell* 66: 154–162.e10